On the Dynamics of Ionic Liquids: Comparisons between Electronically Polarizable and Nonpolarizable Models II

Tianying Yan,*,† Yanting Wang,‡ and Craig Knox§

Institute of New Energy Material Chemistry and Department of Material Chemistry, Nankai University, Tianjin 300071, China, Key Laboratory of Frontiers in Theoretical Physics, Institute of Theoretical Physics, Chinese Academy of Sciences, 55 East Zhongguancun Road, Beijing, 100190, China, and Center for Biophysical Modeling and Simulation and Department of Chemistry, University of Utah, Salt Lake City, Utah 84112-0850

Received: September 15, 2009; Revised Manuscript Received: April 1, 2010

An electronically polarizable model has been developed for the ionic liquid (IL) 1-ethyl-3-methyl-imidazolium nitrate ($EMIM^+/NO_3^-$) (Yan et al. *J. Phys. Chem. B* DOI:10.1021/jp9089112). Molecular dynamics simulations were then performed with both the polarizable and nonpolarizable models. Both models exhibited certain properties that are similar to a supercooled liquid behavior even though the simulations were run at 400 K (89 K above the melting point of $EMIM^+/NO_3^-$). The ionic mean-squared displacement and transverse current correlation function of both models were well represented by a memory function with a fast Gaussian initial relaxation followed by the two-step exponential functions for β- and α- structural relaxations. Another feature shared by both models is the dynamic heterogeneity, which highlights the complex dynamic behavior of ILs. Apart from the overall slow dynamics, the relaxation of the H-atoms attached to the methyl group demonstrates a "free rotor" type of motion. Also, the ethyl group shows the fastest overall relaxation, due to the weak electrostatic interactions on it. Such flexibility enhances the entropic effect and thus favors the liquid state at room temperature. For the dynamical properties reported in this paper, the polarizable model consistently exhibited faster relaxations (including translational and reorientational motions), higher self-diffusion and ionic conductivity, and lower shear viscosity than the nonpolarizable model. The faster relaxations of the polarizable model result from attenuated long-range electrostatic interactions caused by enhanced screening from the polarization effect. Therefore, simulations based on the polarizable model may be analogous to simulations with the nonpolarizable model at higher temperatures. On the other hand, the enhanced intermolecular interactions for the polarizable model at short-range due to the additional charge-dipole and dipole−dipole interactions result in a red shift of the intramolecular C−H stretch spectrum and a higher degree of ion association, leading to a spectrum with enhanced conductivity across the whole frequency range. The vibrational motion associated with the intermolecular hydrogen bonding is highly IR active, highlighting the importance of hydrogen bond dynamics in ILs.

I. Introduction

Room temperature molten salts, or ionic liquids (ILs), are organic salts composed solely of ions. Compared to their inorganic salt counterparts, IL's melting point is much lower and exists at liquid state at room temperature. The reason why ILs are liquids at room temperature is partly due to their bulky and comformationally flexible ions,[1] which lead to small lattice enthalpy and large entropy changes, and such entropic effect favors melting and stabilizes liquid state.[2] The asymmetric cations also make IL to the liquid state with the intermolecular dynamics shifted to lower frequencies than the symmetric cations.[3] However, the deterministic reason why IL is liquid at room temperature is still an open question. ILs are "green" solvents in terms of their low volatility, nonflammability, reusability, and selectivity. Since the properties of ILs can be "tuned" with different combinations of cation, anion, and substitute functional groups, these environmentally benign liquids, also desired as "designer solvents", are promising to replace conventional organic solvents in a variety of applications.[4] Therefore, understanding the interplay of the structure−function relationship is of considerable importance toward the ultimate goal of the systematic design of these charming liquids. At the current state, the unique microscopic physicochemical properties of ILs still remain to be revealed, because the complexity and diversity of ILs raise great challenges to the scientific community. Over the past decade, an increasing amount of studies, including experiments and computer simulations, have been devoted to probe the structural and dynamic properties of this new class of liquids.[5] New liquid state theory and statistical mechanics may be developed to better characterize these complex systems.[6]

Because of their nature of having charged ions, ILs generally exhibit cation−anion association and "remember" their solid state structure[7] although they are liquids at room temperature. For example, these behaviors are seen in the polymorphic structural features of ILs; two different crystalline phases of 1-butyl-3-methylimidazolium hexafluorophosphate ($BMIM^+/PF_6^-$) discovered by calorimetry and X-ray diffraction[8] as well as several phase changes over a narrow temperature range observed in liquid 1-ethyl-3-methylimidazolium butanesulfonate ($EMIM^+/BSO_3^-$) by NMR.[9] As a result, ILs are good glass

* To whom correspondence should be addressed. Tel: (86)22-23505382. Fax: (86)22-23502604. E-mail:tyan@nankai.edu.cn.
† Nankai University.
‡ Chinese Academy of Sciences.
§ University of Utah.

10.1021/jp908914d
Published on Web 05/05/2010

formers and show supercooled behavior over a wide range of temperatures. Besides the spatial heterogeneity described in the accompanying paper,[10] ILs also show dynamic heterogeneity, characterized by the non-Gaussian diffusive behavior at long time scales.[11−13] Computer simulation of $EMIM^+/NO_3^-$ at 400 K, which is 89 K higher than its melting point of 311 K, still shows such behavior.[11] The relaxations of ILs are often described by a stretched exponential, or Kohlrausch−Williams−Watt (KWW) expression, such as in quasielastic neutron scattering (QENS) for the structural relaxation,[14] in dielectric relaxation of collective dipole moment relaxation,[15−17] and in the computer simulation of single particle rotational dynamics,[18−21] a characteristic of glass-forming and supercooled behavior. The temperature dependence of conductivity, diffusion coefficient, and viscosity is often non-Arrhenius and well fit by the Vogel−Fulcher−Tammann (VFT) law,[22−25] as typically observed in glassy or supercooled states. In a broadband dielectric spectroscopy (BDS) and depolarized light scattering (DLS) study on a series of $BMIM^+$ based ILs, it was found that the ionic translational and rotational motions are strongly coupled, because of the high viscosity of ILs.[25] In contrast, a combined dielectric and NMR study on the low viscous $EMIM^+$ based ILs with the bis(trifluoromethane sulfonyl)imide ($TFSI^-$) or dicyanimide [$(CN)_2N^-$] anion found that the reorientational dynamics can be well described by the single-particle reorientation of cations since the static Kirkwood G factor is nearly equal to unity and the collective dynamics has little contribution.[26] Therefore, the versatility of ILs makes them highly desirable as designer solvents.

Triolo and co-workers[27] employed QENS to investigate the structural relaxations of $BMIM^+/PF_6^-$. The time scale ranged from 0.41 to 25 ps, and the temperature ranged from 250 to 320 K. This experiment clearly revealed two relaxation steps, a fast subpicosecond β-relaxation and a slow subnanosecond α-relaxation. The two-step relaxation occurred at all temperatures investigated although $BMIM^+/PF_6^-$ melts at about 280 K.[27] A later QENS study on the same IL identified fast relaxation dynamics associated with methyl group rotation with very low activation energy.[14] The relatively free "rotation" of the methyl group was also detected in a ^{13}C NMR relaxation measurement.[9] A QENS study on pyridinium-based ILs revealed different correlation times for the in-plane and out-of-plane reorientations.[28] Dynamic light scattering of ILs, which probes the density fluctuation over a much larger spatial range than QENS, has also revealed a dynamic, heterogeneous network, characterized by long-range density−density correlation ("cluster mode") and extending from the supercooled state to above the melting point.[29] Holm and co-workers simulated a series of $EMIM^+$ based ILs and found that the translational and rotational relaxations correlated well with hydrogen bond dynamics, illustrating the importance of hydrogen bonds in these systems.[30] In the computer simulation of $BMIM^+/PF_6^-$, the cage correlation function for the ions breaking through a local "cage" surrounding them revealed a two-step structural relaxation.[31]

Femtosecond optical-heterodyne-detected optical Kerr effect (OHD-OKE) spectroscopy or optical-heterodyne-detected Raman-induced Kerr effect spectroscopy (OHD-RIKES),[32] which mainly probes the collective reorientational dynamics, has been recently applied to a variety of ILs[33−36] as well as binary IL mixtures.[37] While the studies by Hyun et al.[33] and Giraud and co-workers[34] were focused on the short-time response within a few picoseconds, Cang and Fayer[35] detected a long-time decay from ∼1 ps to ∼2 ns, reaching the long-time α-relaxation characteristic of organic glass-forming liquids. By measuring the OKE of an IL and its analogous isoelectronic organic binary, Shirota and Castner[38] found that the intermolecular vibrational frequency of the IL is stronger than the latter, which may be attributed to the higher viscosity of the IL. The same authors also found that trimethylsilylmethyl-substituted imidazolium cations reduce shear viscosity tremendously.[39] Using MD simulations, Urahata and Ribeiro compared the calculated density of state (DOS) with the experimentally measured OKE[40] and quasielastic Raman scattering[41] in the low frequency region, in which the reorientation dynamics can be related to the intermolecular vibrational dynamics for the low frequency region. Margulis and co-workers performed some of the first computer simulations of the OKE spectrum.[42] Because of the slow dynamics of ILs, such simulation is extremely time-consuming. To overcome this problem, an approximation was adopted to estimate the dipole-induced-dipole (DID) contribution to the total polarizability in the scattering volume using molecular polarizabilities instead of the conventional atomic polarizabilities. The simulation showed that, besides the rotational dynamics, the cage effect is important even in the long-time decay of the OKE spectrum, in agreement with experiment.[38] Similar DID approximation with molecular polarizabilities was also adopted in Shirota, Ishida, and Nishikawa' study on the comparisons of experimental and simulated OKE spectra.[43,44]

Dielectric spectroscopy probes collective dipole correlations and is complementary to OKE spectroscopy, which probes collective polarization correlations. Weingärtner et al.[15] performed the first dielectric spectroscopy on the ethylammonium nitrate IL between 288.15 and 353.15 K (melting point 287.3 K) and found that there is a distribution of relaxation times and that the dominant relaxation process within the accessible frequency range (3 MHz to 40 GHz) can be explained by the formation of a small amount of dipolar ion complex. The collective response of the ionic network in the neat IL was also found using GHz dielectric spectroscopy.[45] Asaki et al.[46] performed THz transmission spectroscopy on the 1-ethyl-3-methylimidazolium trifluoromethanesulfonate IL and found that there exists a fast Debye-type relaxation, which can be attributed to hydrogen bonding. Because of the conducting nature of ionic liquids, experimental dielectric spectroscopy measures the generalized dielectric spectrum, which has overlapping contributions from both the frequency-dependent dielectric constant $\varepsilon(\omega)$ and the ionic conductivity $\sigma(\omega)$.[47−49] Therefore, caution should be addressed when interpreting such dielectric spectra since the moving ions introduce new degrees of freedom that also contribute to the dielectric response.[16,50] Fortunately, computer simulation can separate the above two contributions. The first computer simulations of dielectric response of ionic liquids were conducted by Steinhauser and co-workers.[51,52] In these simulations, the contribution from the ionic reorientation was estimated from the collective rotational dipole moment, which is determined by subtracting the collective center-of-mass translational dipole moment from the total system dipole moment. The translational and rotational contributions to the static dielectric constant differ for different IL systems,[52] while the cross correlation between them seems to be of negligible importance.[21] On the other hand, the experimental dielectric spectra cannot be solely attributed to the independent ionic rotations, but must take into account the cooperative motion of the ions.[53] Experimentally measured static dielectric constants (ε_0) of ILs typically range between 8 and 16[16,17,50,54] and decrease with increasing alkyl chain length.[50] Thus, ILs may be classified as solvents of moderate polarity, which can be tuned by varying cations and anions.

The slow dynamics of ILs pose a problem for computer simulations. Simulations of tens or even hundreds of nanoseconds are often needed to explore the relaxation process and usually have high computational demands.[42,55−57] Also, because of the complexity of ILs and the difficulty of simulating liquid state properties,[58] most of the current computer simulations are based on conventional nonpolarizable forcefields. Simulations based on nonpolarizable models often predict much lower diffusion coefficient and higher viscosity than experimental values.[13,57,59] Holm and co-workers[60] systematically studied the structural and dynamical properties of two commonly adopted nonpolarizable forcefields, one by Pádua and co-workers[61,62] and another by Wang and co-workers.[63] They found that both forcefields predict too slow dynamics comparing with experimental values.[60] To compensate for the charge screening effect, Morrow and Maginn[31] assigned smaller total charges (0.904e and −0.904e instead of 1e and −1e) to the cation and the anion, respectively, in their MD simulation of $BMIM^+/PF_6^-$. These reduced partial charges mimicked the average charge screening caused by polarization, as well as the charge transfer effects, resulting in self-diffusion coefficients in good agreement with experimental measurements.[23] Similar approaches on the assignment of the reduced partial charges were also conducted by Economou and co-workers on the imidazolium(im)-based ILs and found good agreement with experimental diffusion coefficients.[64] Similarly, Bhargava and Balasubramanian[65] refined Pádua's[62] forcefield parameters for $BMIM^+/PF_6^-$ with reduced partial charges on the ions. The ionic conductivities were found to increase by 3−10-fold, and the agreement with experiment was greatly improved.[65] Since the long-term relaxation of IL is mainly governed by the translational motions of the ions, it is reasonable to see a reduced charge model enhances dynamics, as indicated in an early MD study by Kim and coworkers that the monopolar nature of electrostatic interactions in IL distinguishes itself with polar solvent.[66] By adjusting van der Waals parameters while keeping unit charge on the cations and anions, Soares and co-workers fit a nonpolarizable forcefield that reproduces experimental self-diffusion coefficients and viscosities.[67] It is of interest to note that self-diffusion and viscosity correlate well with van der Waals parameter ε, and reduced ε leads to high self-diffusion and low viscosity. Ludwig and coworkers[68] refined Pádua's[62,69] forcefield parameters of 1,3-alkylimidazoles and fitted the experimental self-diffusion coefficient also with reduced Lennard-Jones interactions. The diffusion coefficients and viscosities were found to be in good agreement with experimental values.[68] On the other hand, it was found that the cohesive energy of the reduced charge model is much lower in both crystal and liquid phases.[70]

It should be emphasized that the above-mentioned nonpolarizable models effectively average the polarization effect. It may be of interest to check if models with reduced charges are able to represent enhanced hydrogen-bonding structure associated with polarizable models.[10] At this moment, a correlation between the structure properties with the transport mechanism is highly desired for this complex system.[71] We developed the first polarizable model for ILs, based on the distributed Thole smeared dipole model.[72] Simulations of the IL $EMIM^+/NO_3^-$ based on the polarizable model had faster diffusion and lower viscosity,[72,73] and lower surface tension,[74] than those with the nonpolarizable model. Smith and co-workers used a similar methodology to develop a polarizable forcefield to simulate the IL *N*-methyl-*N*-propylpyrrolidinium($MPPY^+$)/$TFSI^-$ and obtained good agreement with the experimental diffusion coefficients,[18] and their recent simulations of alkyl- and ether-derivatized imidazolium/$TFSI^-$ based on polarizable forcefield found excellent agreement with experimental diffusion coefficients and viscosities.[75] Initial tests of the polarizable forcefield by Margulis and co-workers have also suggested that polarization leads to faster dynamics.[42] A systematically developed polarizable force field also demonstrated good agreement in terms of transport properties, such as diffusion coefficients, viscosity, conductivity, etc., over many different ILs.[76] The comparison of the polarizable model and the nonpolarizable model for the interface study also reveal that a polarizable model is necessary to capture the surplus of positive charge at the surface, which lowers the surface tension.[74,77] Recently, Tanaka and Siehl developed a fluctuation charge version of a polarizable model for the IL guanidinium chloride,[78] Picĺek et al.[77] and Dang[79] developed a point dipole polarizable forcefield for ILs, and Kato et al. developed a wave function based charge response kernel (CRK) model for ILs,[80] respectively. A shell model of IL developed by Lynden-Bell and Youngs also demonstrate fast dynamics than the nonpolarizable counterpart, and they concluded that the introduction of polarizability is essential for the realistic modeling of dynamics.[70] Such enhanced ionic dynamics associated with polarizable models of inorganic molten salts have been well documented in literature.[81] Compared with polarizable inorganic molten salt models,[82,83] polarizable forcefields for ILs are still immature and developing, and a careful comparison between polarizable and nonpolarizable models of ILs is still desired.

It is somehow surprising to note that the addition of dipole causes fast dynamics of ions, while the total energy of the system decreases with induced polarization. Indeed, it was demonstrated that the presence of electronic polarizability in polar solvent, liquid water, effectively depresses the self-diffusivity of the system.[84] In a recent study, Kato et al. attacked this issue and proposed a nice explanation based on the correlation between the electrostatic energy and induction energy.[80] Specifically, they found that the induction energy tends to be anticorrelated with the electrostatic energy by the permanent charges, and the net result is that energy barrier is effectively lowered for an ion moving from one basin to another. Therefore, ionic motion is accelerated by the polarization effects.

The methodology for developing the polarizable model of ILs and a comparison of the structural properties obtained from the polarizable and nonpolarizable models are given in the accompanying paper.[10] The focus of this paper is on comparing the dynamical properties of these two models. In Section II, the simulation details, which are the same as those detailed in the accompanying paper, are briefly summarized.[10] In Section III, a series of comparisons of the dynamic properties, including dynamic structure factor for the H-atoms (Section III.1) and structural relaxations (Section III.2), are presented. The diffusion characterized by mean-square displacements (MSD) and a proposed memory function are discussed in Section III.3. In Section III.4, the anisotropic relaxation of the polarizability is shown. In Section III.5, electrical conductivity is discussed. In Section III.6, the correlation between the electrostatic energy of the permanent charges and the polarization energy of the induced dipoles for a probe ion (of charge +1e and −1e) is discussed. This paper is summarized in Section IV. The Appendix contains a discussion on estimating shear viscosity with the transverse current correlation function.

II. Simulation Method

Two simulations of an $EMIM^+/NO_3^-$ IL system were performed, one using a polarizable model and the other using

a nonpolarizable model. Detailed descriptions of the polarizable and the nonpolarizable models are given in the accompanying paper.[10] The IL system was the same for both models and consisted of 400 $EMIM^+/NO_3^-$ ion pairs (9,200 atoms) with an all-atom, all-flexible representation. After equilibration at 400 K, which is 89 K higher than the melting point of 311 K, the production runs were performed with constant *NVE* simulation. Periodic boundary conditions (PBC) were applied with a cubic simulation cell. Long-range charge−charge, charge−dipole, and dipole−dipole interactions were handled by Ewald summation with a maximum of eight **k** vectors along each of the three directions in reciprocal space. For the polarizable model, the extended-Lagrangian (ext-L) method for the dipole degrees of freedom was used.[10] The integration time step was 0.4 fs for the polarizable model and 1.0 fs for the nonpolarizable model. The simulations of both models were run for 10 ns with phase space data (velocities, coordinates, and induced dipoles for the polarizable model) sampled every 4 fs.

Simulations with the iteration method for the polarizable model were also run for 1 ns with integration time step 1 fs to compare with the ext-L method for the polarizable model as well as with the nonpolarizable model. Comparisons of ionic MSD for the polarizable model, utilizing both the ext-L and iteration methods, and MSD for the nonpolarizable model, up to 100 ps, are provided in the Supporting Information. It can be seen that the overall trend for the polarizable model does not depend on the choice of integration method, though the MSDs calculated via the iteration method may not converge well with 1 ns MD simulation due to the slow dynamics and dynamical heterogeneity of ILs. Also, the polarizable model, using either integration method, results in faster MSD than the nonpolarizable model.

To study the correlation between the electrostatic energy of the permanent charges and the polarization energy of the induced dipoles, we set up another two simulations by inserting a nonpolarizable bare ion (of charge +1e and −1e) into the polarizable IL model constructed above. The probe ion (ε = 0.24 kcal/mol and σ = 3.49 Å) is the same as that was adopted by Lynden-Bell.[70,85] The simulations with probe ion were run for 2 ns with phase space data sampled every 20 fs.

III. Dynamical Properties

III.1. Dynamic Structure Factor and Vibrational Density of States of the H-Atoms. Quasielastic neutron scattering (QENS) experiments mainly probe incoherent scattering, which represents the loss of the local density self-correlation of the H-atoms.[27] The incoherent dynamic structure factor is given by

$$S(k,\omega) = \mathrm{Re}\int_0^\infty \mathrm{d}t e^{i\omega t} F_s(k,t) \quad (1)$$

where "Re" is the real part operator for a complex variable, and$F_s(k,t)$ is the incoherent intermediate scattering function

$$F_s(k,t) = \langle \exp[i\mathbf{k}\cdot(\boldsymbol{r}_i(t) - \boldsymbol{r}_i(0))]\rangle \quad (2)$$

In the above equation, $\mathbf{k}$ is the wave vector, $\mathbf{r}_i(t)$ is the position of ion i at time t. The angular brackets represent an ensemble average over all ions and over all wave-vectors of the same magnitude.

Figure 1 shows $S(k,\omega)$ and $F_s(k,t)$ for all H-atoms in the IL system at the principal peak position of k = 1.04 Å^{-1} for both the polarizable and nonpolarizable models. Comparing $S(k,\omega)$ for the two models, the polarizable model shows a faster relaxation than the nonpolarizable model. Such a feature can also be seen clearly from the intermediate scattering function. $F_s(k,t)$ for the polarizable model decays much faster than that of the nonpolarizable model. Both models exhibit a distinct two-step relaxation process, a fast β-relaxation followed by a slow α-relaxation. Although simulations were at T = 400 K, a temperature much higher than the ∼311 K melting point, the IL system still showed features of a supercooled liquid, consistent with previous MD simulation study[11] as well as the experimental QENS study of $BMIM^+/PF_6^-$.[27]

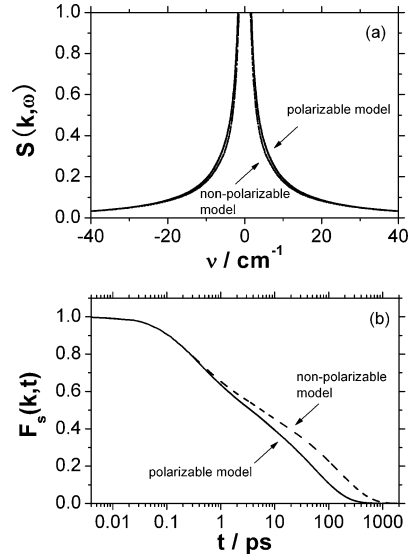

Figure 1. (a) Dynamic structure factor and (b) incoherent intermediate scattering function of all the H-atoms in the system at k = 1.04 Å^{-1} for both the polarizable model (solid line) and the nonpolarizable model (dashed line). The angular frequency is related to the wavenumber by $\omega = 2\pi\nu c$, in which c is the speed of light.

Figure 2 shows $S(k,\omega)$ and $F_s(k,t)$ at k = 1.04 Å^{-1} for individual H-atoms for both the polarizable and nonpolarizable models, respectively. The H2 atom is the most polar H-atom in the system; it forms stronger hydrogen bonds than the other H-atoms and thus moves slower, leading to slow relaxation dynamics. The relaxation curves of the H4 and H5 atoms nearly overlap, indicating similar dynamic relaxation processes for these two H-atoms. The oscillations at ∼0.1 ps for the $F_s(k,t)$ of H2, H4, and H5 shown in Figure 2b,d may be attributed to their librational motion from hydrogen bonds. The H-atoms on the alkyl side-chains all show faster relaxations than those on the imidazolium ring with H8 on the ethyl side-chain showing the fastest relaxation. Interestingly, the H6 atom shows the fastest initial relaxation and then a slower relaxation than the H-atoms on the ethyl side-chain, as can been seen from the line crossings for both $S(k,\omega)$ and $F_s(k,t)$ in Figure 2. The fast initial relaxation of H6 is attributed to the rotational relaxation of the methyl side-chain on the imidazolium ring, which is a free-rotor type motion in the subpicosecond time scale due to its weak hydrogen bond, as discussed in QENS[14] and NMR[9] studies. For the long time scale, the translational motion of the H6 atom follows that of the imidazolium ring and is thus slower than that of the H-atoms on the ethyl side-chain. Therefore, it can be concluded that different H-atoms move on different time scales. This feature is well captured by both the polarizable model and the nonpolarizable model. The overall relaxation of individual H-atoms in the polarizable model is consistently faster than in the nonpolarizable model.

The vibrational density of states (DOS) of the individual H-atoms, whose labels are shown in the inset of Figure 2b, is depicted in Figure 3a−f. The DOS is shown on a semilog plot to emphasize the low frequency portion related to intermolecular motion. The full spectrum of the total H-atom DOS, as well as the low frequency portion, that is, < 350 cm^{-1}, is shown in Figure 3g,h, respectively. The DOS may be compared with IR and Raman/OKE spectroscopy, as will be discussed below. The overall intensity of the polarizable model is slightly lower than that of the nonpolarizable model, similar to the comparison of intensity at higher and lower temperatures. The H-atoms attached to the imidazolium ring exhibit slightly higher frequencies than the alkyl H-atoms, as shown in previous simulations[86] and IR spectra.[87] A distinct feature can be seen in the C−H stretch mode in Figure 3g from 2800 to 3200 cm^{-1}: the polarizable model is "red shifted" compared to the nonpolarizable model. Since the intramolecular forcefield parameters are the same for both models,[10] such red shifting must be caused by the polarization effect. Because of the additional charge−dipole and dipole−dipole interactions, the short-range electrostatic interaction between cations and anions is enhanced, effectively reducing the intramolecular C−H stretching. The low frequency portion of the total H-atom spectrum in Figure 3h also demonstrates a slight red shift for the polarizable model and highlights fast translational and reorientational motion of the polarizable ions. The broad band from 0 to 200 cm^{-1} was also observed in the experimental OKE spectrum.[33,39] The band at ∼500 cm^{-1} is related to the librational motion from intermolecular hydrogen bonding and is strongly IR active, as will be shown below.

III.2. Structural Relaxations. To obtain further information on the structural relaxation, the self-part of the van Hove correlation function was calculated, which can be expressed by the spatial Fourier transform of eq 2 as

$$G_s^{\alpha}(r,t) = \frac{1}{N_{ion}^{\alpha}}\left\langle \sum_{i=1}^{N_{ion}^{\alpha}} \delta[r - |\boldsymbol{r}_i^{cm}(t) - \boldsymbol{r}_i^{cm}(0)|] \right\rangle \quad (3)$$

where $\mathbf{r}_i^{cm}(t)$ denotes the center-of-mass position of the *ith* ion at time t and α denotes the type of the ions, either $EMIM^+$ or NO_3^-. The mean-square displacement (MSD) $\langle \Delta r^2(t) \rangle$ is the second moment of the above probability distribution function.

Figure 4 shows $4\pi r^2 G_s^{\alpha}(r,t)$ for $EMIM^+$ and NO_3^- at nine different values of t for both the polarizable and the nonpolarizable models. The curves are normalized with a unit integration area for better comparison. It can be seen that the polarizable model diffuses much faster than the nonpolarizable model at all time scales. Thus, the ions simulated with the polarizable model are more mobile; the simulation with the nonpolarizable model is qualitatively equivalent to that with the polarizable model at a lower temperature. For both the polarizable and nonpolarizable models, we see that NO_3^- diffuses faster at short time intervals, that is, approximately $t \leq 1000$ ps for the polarizable model and $t \leq 50$ ps for the nonpolarizable model, as shown in Figure 4. At longer time intervals, $EMIM^+$ diffuses slightly faster than NO_3^-. Since the short time quadratic behavior in MSD only lasts less than 0.1 ps,[72] the faster motion of NO_3^- in the short time scale occurs mainly in the intermediate region, possibly because the smaller size of NO_3^- allows for easier breakage of the local "cage". Such non-Gaussian heterogeneous dynamic behavior of $4\pi r^2 G_s^{\alpha}(r,t)$ in the intermediate region has been studied in detail in previous study.[11]

Figure 5 shows $F_s(k,t)$ with several selected wave-vectors for both the polarizable and nonpolarizable models, obtained by eq 2 with the positions of the ions being their center-of-masses, $\mathbf{r}_i(t) = \mathbf{r}_i^{cm}(t)$. A two-step relaxation can be seen from this figure, and the faster relaxation of the polarizable model is also evident. A two-step relaxation was also observed with QENS for $BMIM^+/PF_6^-$ (∼280K melting point) at 320 K.[27] The initial

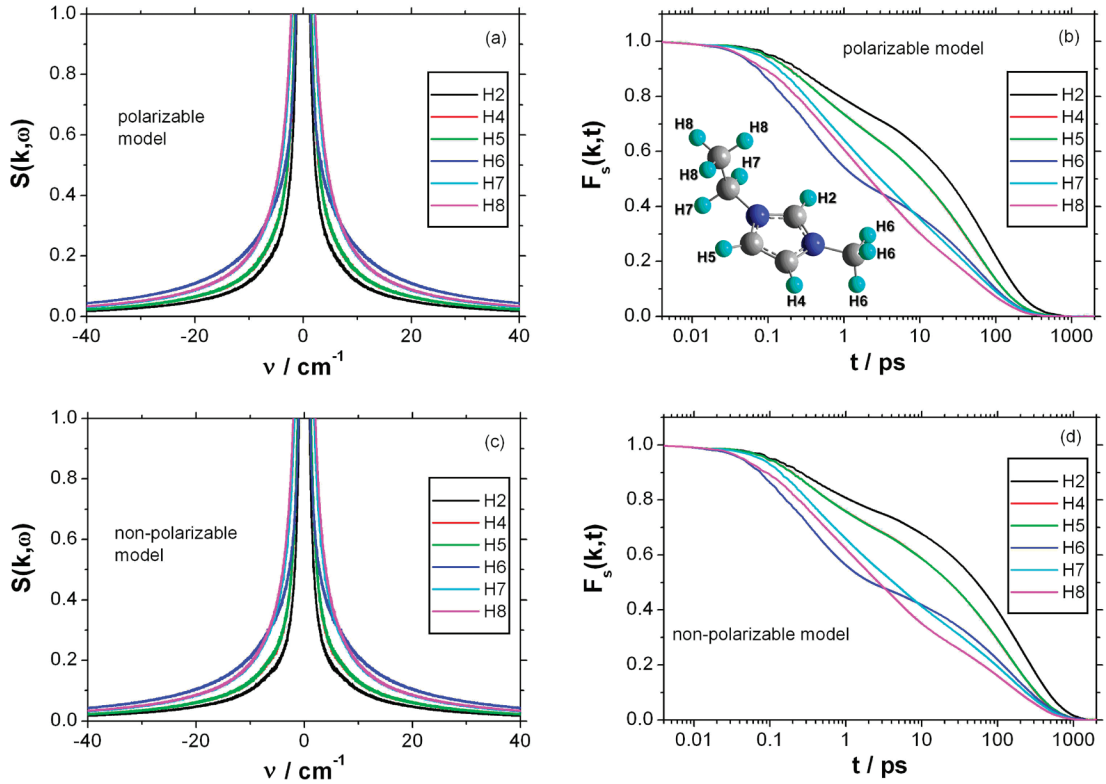

Figure 2. (a) Dynamic structure factor and (b) incoherent intermediate scattering function (right column) of indistinguishable H-atoms for both the polarizable model and the nonpolarizable model. (a) $S(k,\omega)$ for the polarizable model; (b) $F_s(k,t)$ for the polarizable model; (c) $S(k,\omega)$ for the nonpolarizable model; (d) $F_s(k,t)$ for the nonpolarizable model.

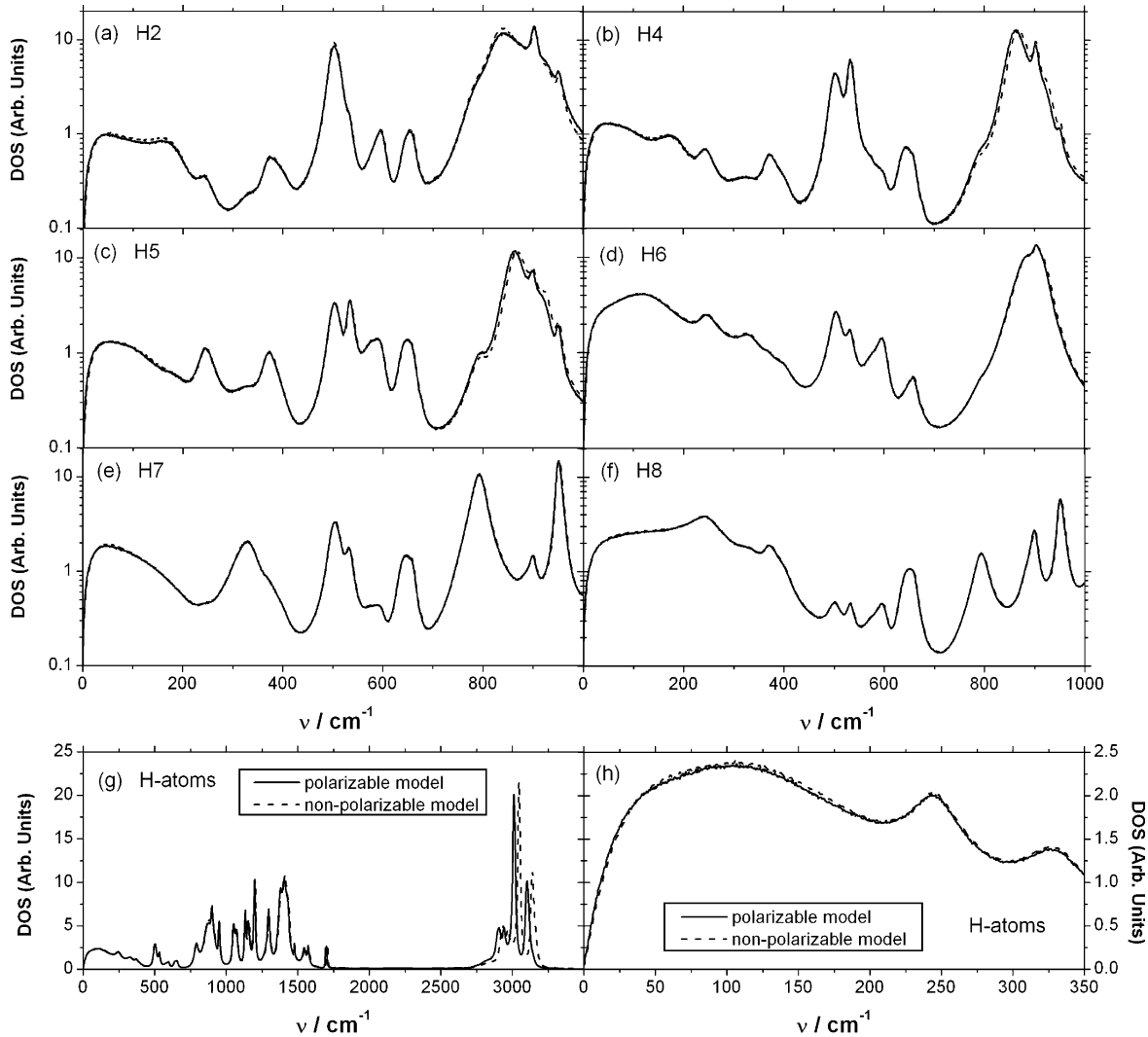

Figure 3. The vibrational density of states (DOS) of the indistinguishable H-atoms for (a) H2; (b) H4; (c) H5; (d) H6; (e) H7; and (f) H8. The full spectrum of total H-atom DOS, as well as the low frequency portion, are shown in (g) and (h), respectively. The spectrum of the polarizable model is shown in solid line, and that of the nonpolarizable model is shown in dashed line. The H-atoms are numerated as the inset of Figure 2b.

fast decay due to the short time quadratic motion in the microscopic region (~0.1 ps) followed by a fast β-relaxation leads $F_s(k,t)$ to a plateau in the intermediate region, which is stretched and more pronounced for the nonpolarizable model. For the final complete decay of $F_s(k,t)$, that is, α-relaxation, the nonpolarizable model takes much longer than the polarizable model.

The presence of the two relaxation processes may be further quantified by the susceptibility spectrum, defined as

$$\chi_s''(k,\omega) = \omega \mathrm{Re} \int_0^\infty \mathrm{d}t e^{i\omega t} F_s(k,t) \qquad (4)$$

where ω is the frequency. Figure 6 shows the frequency-dependent susceptibilities at $k = 1.04$ Å^{-1}, with the inset containing the corresponding $F_s(k,t)$. The first peak for the nonpolarizable model is located at a much lower frequency than the polarizable model, indicating that, for the nonpolarizable model, both α-relaxations occur at a much longer time scale than the polarizable model. The first minimum between the low frequency α-peak and the high frequency microscopic region reflects the β-relaxation plateau in $F_s(k,t)$. The shift of the first minimum to the higher frequency value also indicates a faster β-relaxation for the polarizable model. The shape in the microscopic region, which is characterized by subpicosecond dynamics, is similar for both models. Thus, the major difference for the two models is found to occur at long time relaxations. For the nonpolarizable model, it can be seen from the inset of Figure 6 that the initial decay of $F_s(k,t)$ for the anions is faster than that for the cations. This trend changes at ~50 ps after which the cations decay faster than the anions. For the polarizable model, the anions decay consistently faster than the cations during the whole time window for the specific wavenumber $k = 1.04$ Å^{-1}.

The above analyses demonstrate that the $EMIM^+/NO_3^-$ IL behaves like a supercooled liquid with both the polarizable and nonpolarizable models. Such behavior is more significant with the nonpolarizable model. It should be noted that it is not clear whether a Boson peak exists in the simulation results at 400 K. By taking a closer look at $F_s(k,t)$ for the nonpolarizable model shown in the inset of Figure 6, a weak "bump" can be seen at ~2 ps. Such a "bump" in $F_s(k,t)$ would be represented by a Boson peak in the susceptibility spectrum as a lower frequency shoulder on the second peak. This feature has been observed in many experimental studies of supercooled inorganic molten

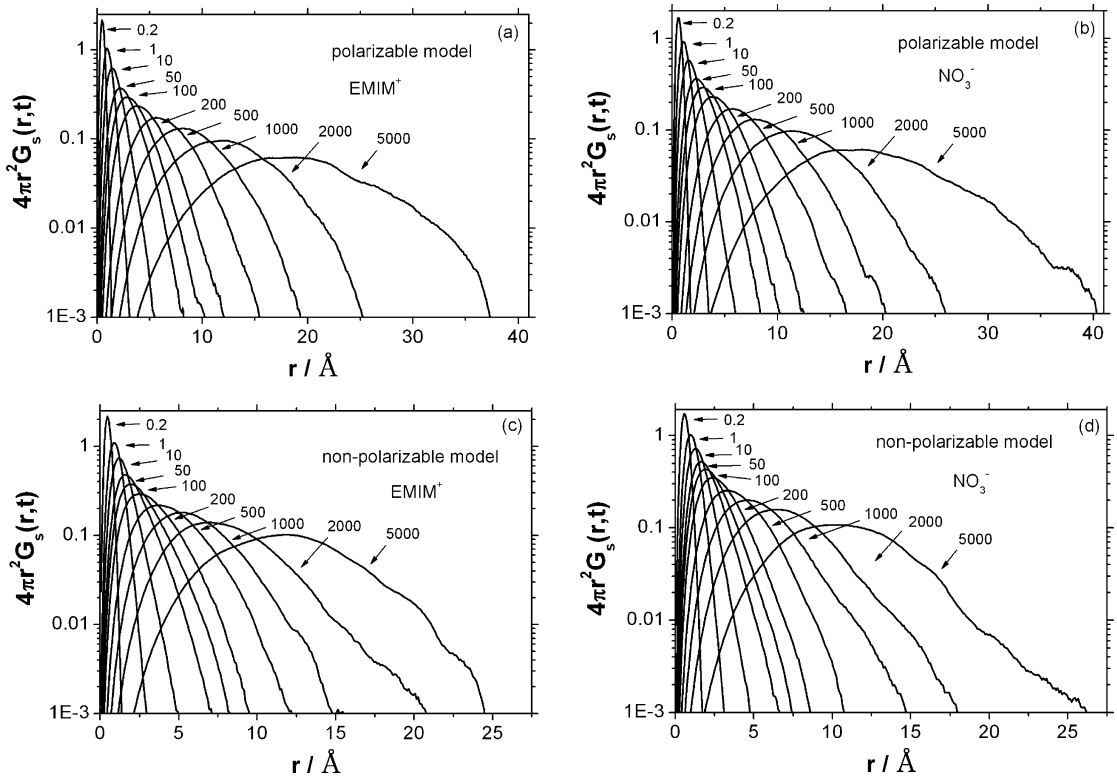

Figure 4. Self-part of the center-of-mass van Hove function at 10 selected time lags (in ps) for both the polarizable model and the nonpolarizable model. (a) $EMIM^+$ of the polarizable model; (b) NO_3^- of the polarizable model; (c) $EMIM^+$ of the nonpolarizable model; (d) NO_3^- of the nonpolarizable model.

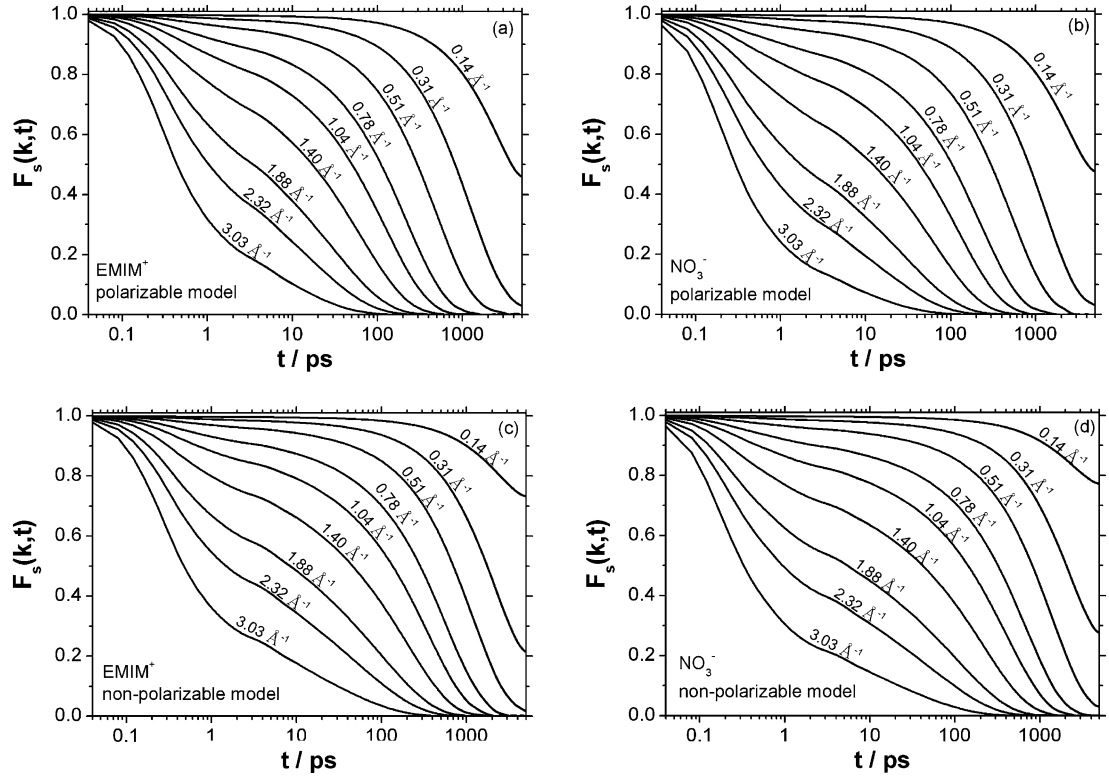

Figure 5. Center-of-mass incoherent intermediate scattering functions at eight wave-vectors, which from the top curve to the bottom curve are 0.14, 0.31, 0.51, 0.78, 1.04, 1.40, 1.88, 2.32, and 3.03 $Å^{-1}$, respectively. (a) $EMIM^+$ of the polarizable model; (b) NO_3^- of the polarizable model; (c) $EMIM^+$ of the nonpolarizable model; (d) NO_3^- of the nonpolarizable model.

salts.[88] However, because of the noise in this susceptibility spectrum, such a feature cannot be clearly identified in this study.

The relaxation of the cation−anion association may be characterized by the distinct part of van Hove correlation function, that is

$$G_d^{\alpha\beta}(r,t) = \left\langle \sum_{i=1}^{N_{ion}^{\alpha}} \sum_{j=1}^{N_{ion}^{\beta}} \delta[r - |\boldsymbol{r}_i^{cm}(t) - \boldsymbol{r}_j^{cm}(0)|] \right\rangle \quad (5)$$

Figure 7 shows the cation−anion $G_d(r,t)$ at several time lags for both the polarizable model and the nonpolarizable model. It can be seen from Figure 7 that the polarizable model fills the repulsive region much quickly than the nonpolarizable model, due to the fast diffusion of the former. Finally, the polarizable model shows a nearly flat $G_d(r,t)$, indicating the decay of the cation−anion associate is completely vanished at 1 ns, while a flat $G_d(r,t)$ is shown at 2 ns for the nonpolarizable model. Therefore, the polarizable model shows much faster relaxation of the cation−anion association than the nonpolarizable model. Furthermore, the simultaneous decaying of the peaks means that the uncorrelated cation and anion diffusions without a preference of a specific cation−anion pair association. Otherwise, the first peak is expected to decay slower than the others. Therefore, the cation−anion association is not likely to last for time longer than nanosecond scale at 400 K, which is in good agreement with the finding of Zhao et al. on similar ILs.[89]

III.3. Mean-Square Displacements. On the basis of the above discussion of the susceptibility spectrum, there are three relaxation steps for the IL system, an ultrafast relaxation within 0.1 ps, followed by a two-step complete structural relaxation, that is, a fast β-relaxation, and then a slow α-relaxation. A two-step phenomenological memory function model was presented in our previous study.[72] Here, a further generalization is made to a three-step memory function, which takes the form

$$\begin{aligned} M(t) &= \omega_0^2[M_1(t) + M_\beta(t) + M_\alpha(t)] \\ &= \omega_0^2[(1 - \beta - \alpha)\exp(-\pi t^2/4\tau_1^2) + \\ &\quad \beta\exp(-t/\tau_\beta) + \alpha\exp(-t/\tau_\alpha)] \end{aligned} \quad (6)$$

where ω_0^2 is the second frequency moment.[81,90] In the above expression, a fast decaying Gaussian function $M_1(t)$ is used to represent the initial ultrafast relaxation, when the dynamical variables lose their memories rapidly. Two slow decaying exponential functions, $M_\beta(t)$ and $M_\alpha(t)$, are used to represent the complete structural relaxations denoted by β- and α-relaxations for the supercooled liquid. Equation 6 has five parameters, β, α_k, τ_{1k}, τ_β, and τ_α, which can be determined by fitting the MSD, given by

$$\langle \Delta r(t)^2 \rangle = \langle |\boldsymbol{r}_i(t) - \boldsymbol{r}_i(0)|^2 \rangle \quad (7)$$

Equation 7 is related to the velocity autocorrelation function (VACF) by $\langle \Delta r(t)^2 \rangle = 6\langle v^2 \rangle \int_0^t dt'(t - t')C_v(t')$, where $C(t) = \langle \mathbf{v}(t)\cdot\mathbf{v}(0)\rangle/3\langle v^2\rangle$ is the normalized VACF and $\langle v^2 \rangle = k_B T/m$. Following the memory function approach, that is, $\dot{C}(t) = -\int_0^t dt' M(t - t')C(t')$, the above convolutions may be solved by taking the Laplace transform on both sides and then taking the inverse to give

$$\langle \Delta r(t)^2 \rangle = 6\langle v^2 \rangle \mathcal{L}^{-1}\left[\frac{1}{s^2(s + \tilde{M}(s))}\right] \quad (8)$$

where $\mathcal{L}^{-1}$ denotes the inverse Laplace transform, and s is the Laplace variable. The Laplace transform of $M(t)$ defined in eq 6 may be written as

$$\begin{aligned} \tilde{M}(s) &= \omega_0^2[\tilde{M}_1(t) + \tilde{M}_\beta(t) + \tilde{M}_\alpha(t)] \\ &= \omega_0^2[(1 - \beta - \alpha)\tau_1 \exp(\tau_1^2 s^2)\mathrm{erfc}(\tau_1 s/\pi^{1/2}) + \\ &\quad \frac{\alpha\tau_\beta}{1 + \tau_\beta s} + \frac{\alpha\tau_\alpha}{1 + \tau_\alpha s} \end{aligned} \quad (9)$$

where $\omega_0^2 = \langle i^2/v^2 \rangle$ is calculated via MD simulation and $\mathrm{erfc}(\tau_1 s/\pi^{1/2})$ is the complementary error function. The inverse Laplace transform in eq 7 is solved numerically by Stehfest's algorithm.[91] The MSD in eq 8 is fitted with the parameters (β, α_k, τ_{1k}, τ_β, and τ_α) to the MSD from the MD simulation given by eq 7. A similar procedure has been applied to the MSD of the $BMIM^+/PF_6^-$ IL by Margulis et al.[92]

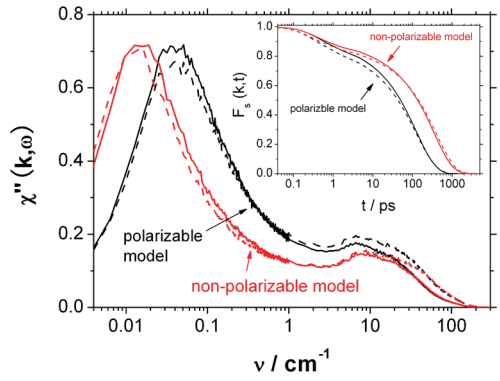

Figure 6. Frequency-dependent susceptibility at the wave vector of 1.04 Å^{-1}, which is close to the principal peak in the static structure factor for both the polarizable model (red line) and the nonpolarizable model (blue line), in which both the $EMIM^+$ (solid line) and NO_3^- (dashed line) are shown. The inset shows the intermediate scattering function at the same wave vector.

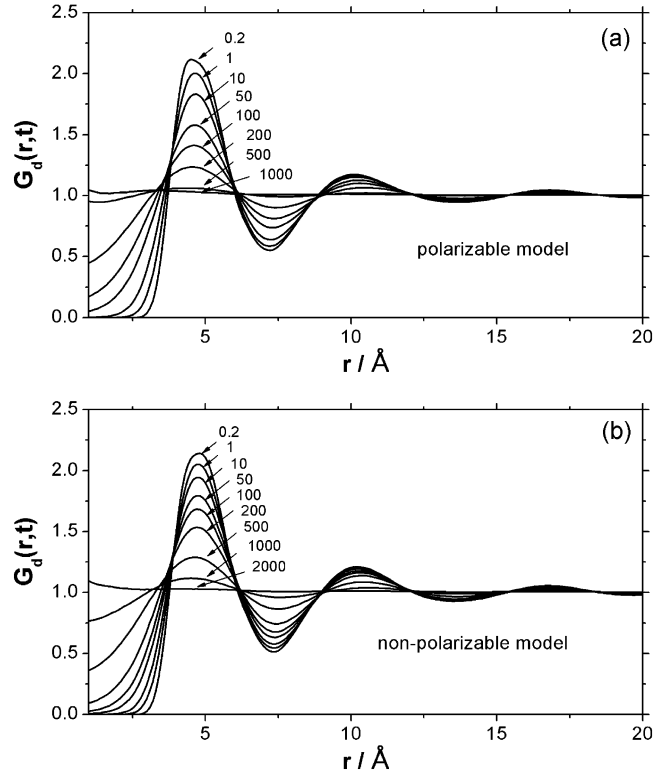

Figure 7. Distinct part of the center-of-mass van Hove function at selected time lags (in ps) for both the polarizable model and the nonpolarizable model. (a) $EMIM^+/NO_3^-$ of the polarizable model; (b) $EMIM^+/NO_3^-$ of the nonpolarizable model.

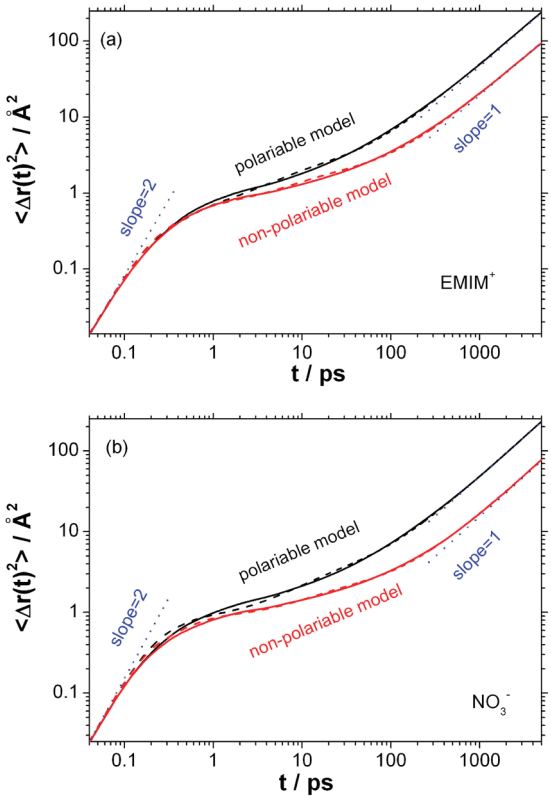

Figure 8. Mean-squared displacements of $EMIM^+$ (a) and NO_3^- (b) for the polarizable model (black line) and the nonpolarizable model (red line) in which the solid line denotes the MSD estimated by eq 6 from the MD simulations and the dashed line denotes the fitted MSD of eq 7 by utilizing the memory function given by eq 5. The blue dotted lines with slope = 1 and slope = 2 are guides for the eye, which mark the regions corresponding to $\langle \Delta r(t)^2 \rangle \propto t$ and $\langle \Delta r(t)^2 \rangle \propto t^2$, respectively.

The mean-square displacements (MSD), given by eq 7, are shown in Figure 8 as log−log plots for $EMIM^+$ and NO_3^-, respectively. The ultrafast initial relaxation that obeys $\langle \Delta r(t)^2 \rangle \propto t^2$ (characterized by slope = 2 in the log−log plot) lasts only ~0.1 ps for both the polarizable and nonpolarizable models. However, at longer time scales, the self-diffusion of the two models is quite different. At the longest time scale of 2 ns for the MSD calculations, the MSD of the polarizable model is about 2.5−3 times larger than that of the nonpolarizable model, consistent with our previous study.[72] Comparison of the MSD estimated by the polarizable model, in which the induced dipoles were calculated with the iteration method[10] and the system was "locked" on the desired Born−Oppenheimer surface, shows similar trends, as demonstrated in the Supporting Information. The intermediate region may be understood by the combination of the two-step structural relaxation as described above. The relaxation at the long time scales is dominated by α-relaxation, and the MSD eventually approaches the slope = 1 region with $\langle \Delta r(t)^2 \rangle \propto t$. It should be noted that the self-diffusion coefficients listed in Table 1 are smaller than those reported previously.[72] Considering the slow dynamics and dynamical heterogeneous behavior of the system[11] as well as the longer MD simulations of this study (10 ns compared to 1.2 ns in our previous study), the MSD results of this study should be better converged and more accurate. However, caution should be exercised when interpreting the self-diffusion coefficients listed in Table 1 because much longer MD runs may be needed to get fully converged self-diffusion coefficients. In a MD simulation of a pyridinium-based IL from 298 to 423 K, Maggin and co-workers demonstrated the difficulty of getting reliable self-diffusion coefficients from simulations as long as 20 ns; even for the longest reported times, the system still exhibited subdiffusive behavior.[13]

The fits given by eq 8 for both the polarizable and nonpolarizable models are also shown in Figure 8 with the fitted parameters listed in Table 1. It can be seen that the memory function proposed in eq 6 fits MSD reasonably well up to 5 ns and is comparable to the fitting done by Margulis et al.[92] From the fitted parameters given in Table 1, it can be seen that the relaxation times τ_β and τ_α of the polarizable model are smaller than those of the nonpolarizable model, indicating that the β- and α- relaxations for the polarizable model are faster than those for the nonpolarizable model, while the small τ_1 for both models indicates that the initial ultrafast relaxation of the ions explores the local potential energy basin area. The fitted parameters are listed in Table 1, along with the self-diffusion coefficients estimated by the Einstein relation $D = (1/6)\mathrm{d}\langle \Delta r(t)^2 \rangle / \mathrm{d}t$ and those estimated by $D = \langle v^2 \rangle / \tilde{M}(0)$[90] with

$$\tilde{M}(0) = \omega_0^2[(1 - \beta - \alpha)\tau_1 + \beta\tau_\beta + \alpha\tau_\alpha] \qquad (10)$$

The self-diffusion coefficients computed with the above two methods agree well with each other for both the polarizable and nonpolarizable models, indicating reasonably good fitting. It is interesting to note that the self-diffusion coefficient of the cation is slightly smaller than that of the anion for the polarizable model, while the opposite is true for the nonpolarizable model. According to the self-diffusion coefficients estimated by the Einstein relation from the MD simulation data, which are listed in Table 1, the cationic transference numbers, $D_{\mathrm{cation}}/(D_{\mathrm{cation}} + D_{\mathrm{anion}})$, are 0.51 for the polarizable model and 0.56 for the nonpolarizable model. The experimental study[24] by Watanabe and co-workers on $C_nMIM^+/TFSI^-$ with $n = 2-8$ shows that the cationic transference number is larger than 0.5 over the temperature range from 260−350 K, but the temperature versus cationic transference number plot has a negative slope, indicating that the rate of change, $\mathrm{d}D_{\mathrm{anion}}/\mathrm{d}T$, of the self-diffusion coefficient of the anion is larger than that of the cation. Watanabe attributes the large cationic transference number to the planar structure of the imidazolium ring. In the simulations of this study, the anion NO_3^- was also planar, possibly reducing the transference number. Therefore, for the $EMIM^+/NO_3^-$ IL, it seems reasonable that the cationic transference number is close to 0.5, that is, nearly equal self-diffusion coefficients for both the cation and the anion. Also, if the polarizable model behaves as if it were run at a higher temperature than the nonpolarizable model, the rate of change of the anion's self-diffusion should be larger than that of the cation, as consistent with the 0.51 and 0.56 cationic transference numbers, respectively, for the polarizable and nonpolarizable models.

In our previous study[72] of the same IL system, a two-step phenomenological memory function kernel was proposed and fit to the transverse current correlation function, from which the shear viscosity was estimated. In the current study, a second generation polarizable model has been developed, and a three-step memory function has been proposed. Thus, a re-examination of viscosity is also desired with the three-step memory function given in eq 6. The shear viscosities estimated via eq 6 are higher than the values reported previously, especially for the nonpolarizable model, as shown in the Appendix.

The center-of-mass velocity autocorrelation functions (VACF) $C_v(t) = \langle \mathbf{v}^c(t) \cdot \mathbf{v}^c(0) \rangle / 3\langle v^{c2} \rangle$, in which $\mathbf{v}^c(t)$ denotes the COM

TABLE 1: The Fitted Parameters of MSD and Self-Diffusion Coefficient

	Polarizable model							
	ω_0^2 (ps^{-2})[a]	β	α	τ_1 (ps)	τ_β (ps)	τ_α (ps)	D (Å^2 ps^{-1})[b]	D (Å^2 ps^{-1})[c]
$EMIM^+$	182.7	4.52×10^{-2}	8.98×10^{-2}	7.77×10^{-2}	1.81	39.95	7.80×10^{-3}	8.05×10^{-3}
NO_3^-	216.2	4.42×10^{-2}	0.125	6.27×10^{-2}	3.50	61.64	7.68×10^{-3}	7.71×10^{-3}
	Nonpolarizable model							
	ω_0^2 (ps^{-2})[a]	β	α	τ_1 (ps)	τ_β (ps)	τ_α (ps)	D (Å^2 ps^{-1})[b]	D (Å^2 ps^{-1})[c]
$EMIM^+$	185.4	5.59×10^{-2}	7.68×10^{-2}	7.12×10^{-2}	3.76	84.93	3.09×10^{-3}	3.16×10^{-3}
NO_3^-	226.4	7.19×10^{-2}	8.91×10^{-2}	7.50×10^{-2}	6.50	121.06	2.61×10^{-3}	2.53×10^{-3}

[a] $\omega_0^2 = \langle \dot{v}^2/v^2 \rangle$ is calculated by taking the numerical derivatives of the MD simulation data. [b] Self-diffusion coefficient calculated by $D = \langle v^2 \rangle / \tilde{M}(0)$, where $\tilde{M}(0)$ is given by eq 10 with the fitted parameters in this table and $\langle v^2 \rangle = k_B T/m$. [c] Self-diffusion coefficient calculated by $D = \langle \Delta r(t)^2 \rangle / 6t$, where $\langle \Delta r(t)^2 \rangle$ is given by eq 7.

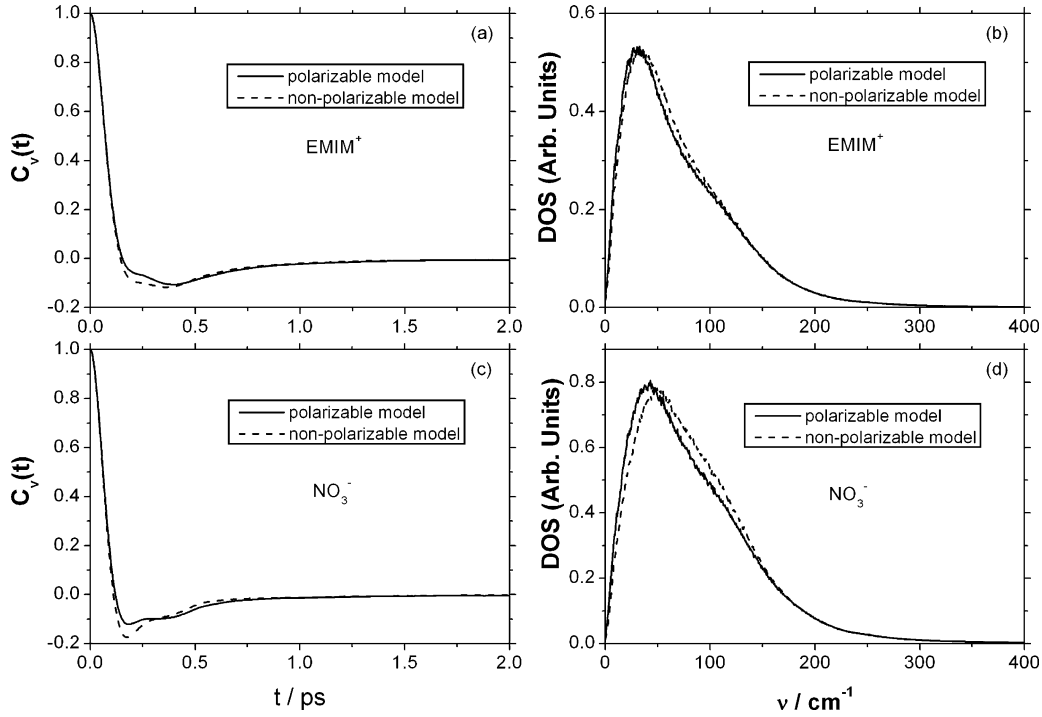

Figure 9. Center-of-mass velocity autocorrelation functions for $EMIM^+$ (a) and NO_3^- (c) for the polarizable (solid line) model and the nonpolarizable model (dashed line). Their Fourier transforms for the density of states are shown in (b) and (d), respectively.

velocity at time t, as well as its Fourier transform−vibrational density-of-states (DOS), for both the polarizable and nonpolarizable models, are given in Figure 9. It can be seen that the minimum of the VACF for the polarizable model is shallow and occurs at a later time than that for the nonpolarizable model, indicating that the local cage effect is less pronounced for the polarizable model. The low frequency peak is associated with the collective motion of the ions, and the shoulder at $\sim$100 cm^{-1} corresponds to single ion motion as the ions rattle in the local cage. The translational motion caused by the intermolecular interactions shifts to lower frequencies due to screening of long-range electrostatic interactions, similar to a study at high and low temperatures.[42] The spectral shift to the lower frequencies for the polarizable model implies the weaker intermolecular interactions compared with the nonpolarizable model.[43] Thus, the presence of electric polarization makes the model softer and easier to escape from the local cage.

III.4. Polarizability Anisotropic Relaxation. The frequency domain depolarized light scattering (DLS), or equivalently the time domain optical Kerr effect (OKE),[32] can probe the fluctuation of the collective polarizability, $\Pi_{xz}(t)$ within the scattering volume from which the system dynamic information can be probed. In the condensed phase, the molecular polarizabilities of the interacting molecules are different from those of the isolated molecules due to the collision induced (CI) effect, which is known to be important.[93] This complicates the situation because in experiments it is difficult to separate the CI signal from those contributed by the collective orientation relaxation of the molecules.[94] It was found that the CI polarizability makes a substantial contribution to the DLS signal on all relevant time scales.[94,95] In computer simulation, the separation of these two contributions may be estimated by the dipole-induced-dipole (DID) approximation.[94−96] As the molecules interact with each other, their molecular polarizability should be different than their isolated molecular polarizability due to the CI effect, and the effective polarizability may be written as[97]

$$\boldsymbol{\alpha}_i^{(n)} \cong \boldsymbol{\alpha}_i + \boldsymbol{\alpha}_i^{(n-1)} \sum_{j \neq i}^{N_{\mathrm{mol}}} \boldsymbol{T}_{ij} \tilde{\boldsymbol{\alpha}}_j \tag{11}$$

where the CI effect is calculated iteratively, that is, the all-DID approximation. Because of the extreme computational demand for estimating DID with atomic polarizability, the anisotropic molecular polarizability in eq 11 is adopted, similar to Margulis[42]

and Ishida's[44] treatment of a similar IL system. Therefore, in the above expression, $\alpha_i^{(n)}$ is the effective molecular polarizability of the ith molecule after the nth iteration, $\boldsymbol{\alpha}_i$ is the isolated molecular polarizability given by eq 6 of the accompanying paper,[10] and $\tilde{\boldsymbol{\alpha}}_j$ represents the molecular polarizability of the jth molecule, which could be the result after the nth or $(n-1)$th iteration depending on the order of the update. For a system of rather high molecular polarizability (c.f. Table 1 of the accompany paper[10]), it was found that it is difficult to get the converged molecular polarizability by using a point dipole model.[98] Therefore, in eq 11, $\mathbf{T}_{ij}$ is still subjected to Thole smearing and calculated by eq 7 in the accompanying paper,[10] in which α_i and α_j are instead given by the isotropic molecular polarizability, that is, $\alpha_i = Tr\langle\boldsymbol{\alpha}_i\rangle/3$, for the Thole smearing factor $A_{ij} = (\alpha_i\alpha_j)^{1/6}$. It should be noted that only in determining A_{ij} the isotropic molecular polarizability α_i scalar was used, while in eq 11 the molecular polarizability $\boldsymbol{\alpha}_i$ is a tensor. Similar approach was also adopted in Ishida and co-workers' study,[44] but with a different Thole smearing function (linear decay vs exponential decay in this study) to prevent the induced dipole from divergence with all-order DID approximation. By using a convergence criterion $\sum_{i=1}^{N_{mol}}\sum_{y=1}^{3}\sum_{z=1}^{3}(\alpha_{yz,i}^{(n)} - \alpha_{yz,i}^{(n-1)})^2/9N_{mol} \le 10^{-6}$, where $\alpha_{yz,i}^{(n)}$ is the yz Cartesian component of the molecular polarizability tensor of the ith molecule after the nth iteration, eq 11 usually converges in 6−8 cycles. Equation 11 can be applied on both the polarizable and nonpolarizable models. For the latter, the atomic polarizabilities given in Table 1 of the accompanying paper were adopted.[10] In this study, it was found that the ratio of the effective isotropic molecular polarizability to the isolated molecular polarizability was between 93.5 to 94.1% for the $EMIM^+$ and NO_3^- for both the polarizable and nonpolarizable models.

From eq 11, the collective polarizability within the scattering volume can thus be separated into two contributions, one from the isolated molecular polarizability and the other from the CI polarizability, such as

$$\boldsymbol{\Pi} = \boldsymbol{\Pi}^M + \boldsymbol{\Pi}^I = \sum_{i=1}^{N_{mol}} \boldsymbol{\alpha}_i + \sum_{i=1}^{N_{mol}}\sum_{j\neq i}^{N_{mol}} \boldsymbol{\alpha}_i^{(n)} \boldsymbol{T}_{ij} \boldsymbol{\alpha}_j^{(n)} \quad (12)$$

The third-order nonlinear response of the system probed by the OKE consists of two parts, the zero-time electronic response, which may be represented as a delta function and which contains no information about molecular dynamics,[99] and the longer time nuclear response.[32,97,99,100] The anisotropic polarizability response function, probed by the depolarized Raman scattering, may be written as[95,96,98,99]

$$\begin{aligned} R_{\text{aniso}}^{(3),\text{nuc}}(t) &= -\frac{\theta(t)}{k_B T}\frac{\partial}{\partial t}\langle \Pi_{yz}(t)\Pi_{yz}(0)\rangle \\ &= -\frac{\theta(t)}{k_B T}\frac{\partial}{\partial t}(\langle \Pi_{yz}^{M}(t)\Pi_{yz}^{M}(0)\rangle + \\ &\quad 2\langle \Pi_{yz}^{M}(t)\Pi_{yz}^{I}(0)\rangle + \langle \Pi_{yz}^{I}(t)\Pi_{yz}^{I}(0)\rangle) \\ &= R^{MM}(t) + R^{MI}(t) + R^{II}(t) \end{aligned} \quad (13)$$

where Π_{yz} is the off-diagonal Cartesian component of eq 12 and $\theta(t)$ is the heaviside function. Equation 13 contains the autocorrelation of the isolated molecular polarizability and CI polarizability, as well as the cross-correlation between them.

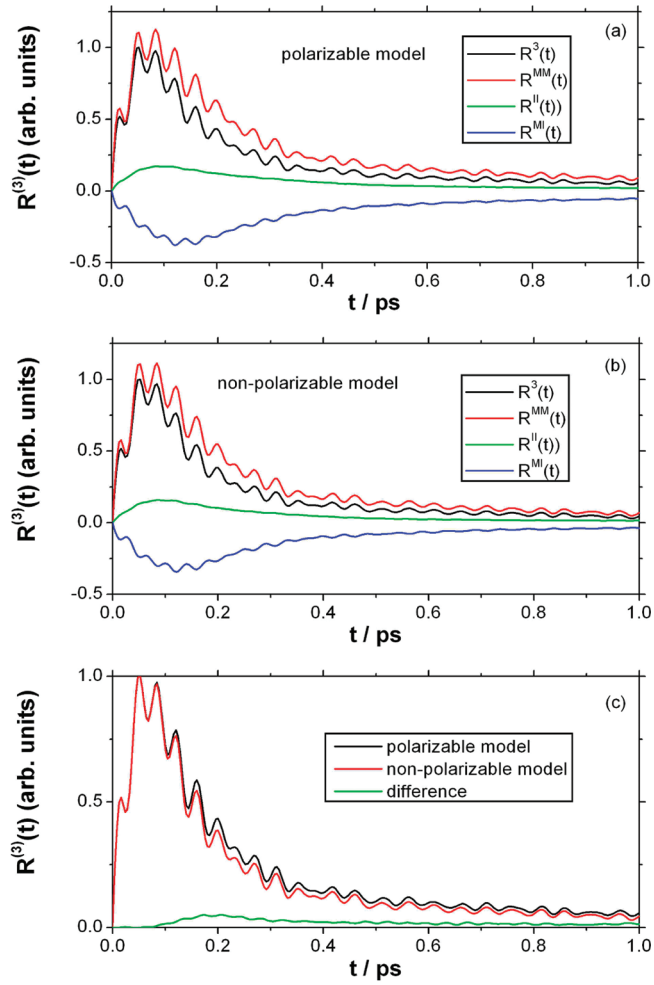

Figure 10. Anisotropic nuclear OKE response function within 2 ps. (a) The polarizable model with the total $R_{\text{aniso}}^{(3),\text{nuc}}(t)$ (black) and the individual responses, $R^{MM}(t)$ (red), $R^{II}(t)$ (green), and $R^{MI}(t)$ (blue); (b) the nonpolarizable model with the total and the individual responses; (c) comparison of the total nuclear OKE response functions for the polarizable model (black), nonpolarizable model (blue), and the difference $R_{\text{aniso}}^{(3),\text{nuc}}(t)_{\text{polarizable}} - R_{\text{aniso}}^{(3),\text{nuc}}(t)_{\text{nonpolarizable}}$ (green).

The real-time OKE response functions given by eq 13 for both the polarizable and nonpolarizable models are shown in Figure 10, in which the high frequency ($\nu > 1000$ cm^{-1}) contributions are filtered out. The contributions from different correlations are also shown. It can be seen that the CI polarizability contributions are across the entire time window with the molecular polarizability, and the cross-correlation between CI and molecular polarizability attenuates the total response function. Therefore, the CI and molecular contributions to the OKE signal are strongly coupled.

For the response functions shown in Figure 10, a peak within ~10 fs for both models is well separated from the rest of the signal. This fast response may be attributed to the intramolecular vibrational motions due to bond stretching. Experimentally, this fast response may possibly merge into the zero-time instantaneous electronic response. Apart from that, the response functions contain the high-frequency underdamped oscillations, with a period of ~0.037 ps (~900 cm^{-1}), superimposed on the slowly varying damped responses for the collective liquid response. The frequency for the above oscillation corresponds to the intramolecular bending modes. The occurrence of the broad main peak around 0.06 − 0.12 ps corresponds to the experimental one and is due to nuclear response to the ultrafast librational dynamics, found in the experimental studies of

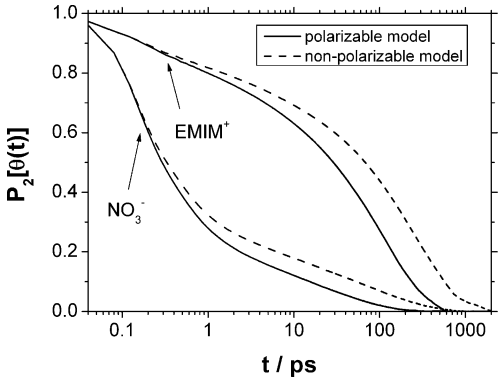

Figure 11. Orientational relaxation function $P_2[\theta(t)]$ for $EMIM^+$ and NO_3^-, where $\theta(t)$ is the angle between the unit vector $\boldsymbol{u}$ perpendicular to the molecular plane at time 0 and time t.

$C_nMIM^+/TFSI^-$ with $n = 2-10$[33] and $BMMIM^+/TFSI^-$[34] at room temperature.

Figure 10c shows the comparison of the total response functions for the polarizable and nonpolarizable models in a semilog plot. While the initial ultrafast response below 0.1 ps, which is characteristic of the intramolecular vibrational and librational motions, is similar for both models, the polarizable model shows a stronger signal at longer time in the subpicosecond time scale. Since OKE measures the negative time derivatives of the polarizability-polarizability time correlation function, or equivalently, the negative time derivatives of the collective orientational correlation function for the long time tail,[101] the stronger signal at the long time tail indicates a faster relaxation of the molecular reorientation for the polarizable model. Experimental studies show that $C_5MIM^+/TFSI^-$ has a stronger signal than $C_8MIM^+/TFSI^-$,[33] and the 1-methoxyethylpyridinium dicyanoamide ($MOEPy^+/DCA^-$) IL also has a stronger signal than its analogous isoelectronic charge neutral organic binary mixture, due to the slower reorientational relaxation of the bulky C_8MIM^+ and the charged IL $MOEPy^+/DCA^-$. In both cases, the sample with a faster orientational relaxation exhibits a stronger signal at the subpicosecond time scale.

To gain further insight, the reorientational relaxation was calculated, as defined by the second Legendre polynomial as

$$P_2[\theta(t)] = \frac{1}{2}\langle 3\cos^2\theta(t) - 1\rangle = \frac{1}{2}\langle 3[\boldsymbol{u}(t)\cdot\boldsymbol{u}(0)]^2 - 1\rangle \tag{14}$$

where $\boldsymbol{u}(t)$ is defined as the unit vector perpendicular to the molecular plane, which accounts for the largest change in the molecular anisotropic polarizability, at time t (see Figure 4 of the accompanying paper[10]). Figure 11 shows the self-reorientational relaxations for the cations and anions. The distinct difference between the two models is that the reorientational relaxations for the polarizable model are much faster than those for the nonpolarizable model, consistent with the OKE signal shown in the inset of Figure 10c. Another feature is that the reorientational motion of NO_3^- relaxes much faster than $EMIM^+$, due to the smaller ion size of NO_3^-.

The response function expressed in the frequency domain is given by the imaginary part of the Fourier transform of eq 13, as[32,99]

$$-\mathrm{Im}[\chi(\omega)] = -\mathrm{Im}\int_0^\infty \mathrm{d}t e^{i\omega t} R^{(3),\mathrm{nuc}}_{\mathrm{aniso}}(t) = \omega I_{\mathrm{DLS}}(\omega) \tag{15}$$

where $I_{\mathrm{DLS}}(\omega) \propto \mathrm{Re}\int_0^\infty \mathrm{d}t e^{i\omega t}\langle\Pi_{yz}(t)\Pi_{yz}(0)\rangle$ is the intensity of DLS at frequency ω.[34,102] This definition contains information of the polarizability fluctuations. Considering the Bose-Einstein correction, eq 15 may be written as[32,99] $-\mathrm{Im}[\chi''(\omega)] = (1 - e^{-\hbar\omega/k_{\mathrm{BT}}})I_{\mathrm{DRS}}(\omega)$, which reduces to eq 15 by considering $-\mathrm{Im}[\chi''(\omega)] \propto \omega I_{\mathrm{DLS}}(\omega)$ in the classical high-temperature limit.

Figure 12a,b shows the total response functions in the frequency domain for both the polarizable and nonpolarizable models. The spectra show a rapid peak at $\sim$10 cm^{-1} and a broad band extending to $\sim$300 cm^{-1}. The full-width-half-maximum (fwhm) is $\sim$160 cm^{-1}. The difference in the spectrum between the polarizable and nonpolarizable models is shown in Figure 11c as a semilog plot. It can be seen that the major difference between the two models arises at the low frequency region, attributed to the fast diffusive reorientation of the polarizable ions.[99] As shown in Figure 3 for the vibrational density of states (DOS) of individual H-atoms, the bands at $\sim$240, $\sim$330, and $\sim$375 cm^{-1} in the response spectra may be attributed to the intramolecular bending motions of the methyl and ethyl groups,[103] which can be seen clearly in Figure 3g,h. The weak band at $\sim$500 cm^{-1} is strongly IR active, as shown in the next section. The weak band at 535 cm^{-1} is attributed to the twisting of the imidazolium ring, when H4 and H5 make a dominant contribution. The bump at 595 cm^{-1} is due to the twist motion of the imidazolium ring involving H2, H5, and H7. The band at 665 cm^{-1} in Figure 11c may be attributed to the torsional motion involving C5−(C7, C8)−C2−N1, which is verified by the fact that H5, H2, H7, and H8 make the main contribution for this band, as seen in Figure 3g,h. The broad band at 800−1000 cm^{-1} is associated with the intramolecular motions of the imidazolium ring.[103]

III.5. Ionic Conductivity. The conductivity spectrum for the nonpolarizable model may be written as

$$\sigma(\omega) = \frac{1}{3k_{\mathrm{B}}TV}\int_0^\infty \mathrm{d}t e^{i\omega t}\langle\boldsymbol{J}(t)\cdot\boldsymbol{J}(0)\rangle = \frac{1}{3k_{\mathrm{B}}TV}\langle\boldsymbol{J}(t)\cdot\boldsymbol{J}(0)\rangle_\omega \tag{16}$$

where $\boldsymbol{J}(t) = \sum_{i=1}^N q_i\mathbf{v}_i(t)$ is the total charge current of the system at time t. For the polarizable model, an additional term due to the induced dipole is added, so that the conductivity spectrum for the polarizable model may be written as[48,82,104]

$$\begin{aligned}\sigma(\omega) &= \frac{1}{3k_{\mathrm{B}}TV}\langle[\boldsymbol{J}(t) + \dot{\boldsymbol{m}}(t)]\cdot[\boldsymbol{J}(0) + \dot{\boldsymbol{m}}(0)]\rangle_\omega \\ &= \frac{1}{3k_{\mathrm{B}}TV}(-i\omega\langle m^2\rangle + \langle\boldsymbol{J}(t)\cdot\boldsymbol{J}(0)\rangle_\omega + \\ &\quad 2i\omega\langle\boldsymbol{J}(t)\cdot\boldsymbol{m}(0)\rangle_\omega + \omega^2\langle\boldsymbol{m}(t)\cdot\boldsymbol{m}(0)\rangle_\omega)\end{aligned} \tag{17}$$

where $\boldsymbol{m}(t) = \sum_{i=1}^{N_{\mathrm{atoms}}}\boldsymbol{\mu}_i(t)$ is the total induced dipole in the system at time t. The phase space time reversible symmetry for the correlation function,[93] that is, $\langle\dot{\boldsymbol{m}}(t)\cdot\boldsymbol{J}(0)\rangle = \langle\boldsymbol{J}(t)\cdot\dot{\boldsymbol{m}}(0)\rangle$ and $\langle\boldsymbol{m}(t)\cdot\boldsymbol{J}(0)\rangle = -\langle\boldsymbol{J}(t)\cdot\boldsymbol{m}(0)\rangle$, are used to obtain eq 16. Equations 16 and 17 may also be interpreted as the far-infrared (FIR) spectrum without the Bose-Einstein correction in arbitrary units.[82,104,105]

Figure 13 shows the real part of the conductivity spectrum, given by eq 16 and 17, for both the polarizable and nonpolar-

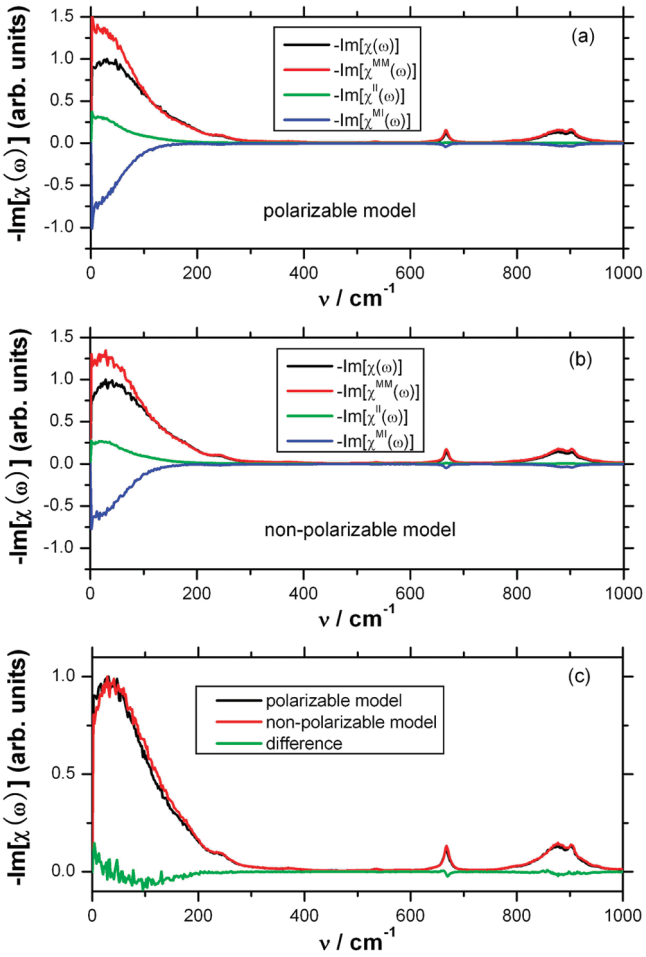

Figure 12. The negative imaginary part of the Fourier transform of the total nuclear OKE response functions. (a) The polarizable model with the total−Im [$\chi(\omega)$] (black), and individual contributions by Fourier transformation of the individual contributions in eq 12, −Im [$\chi^{MM}(\omega)$] (red), −Im [$\chi^{II}(\omega)$] (green), and −Im [$\chi^{MI}(\omega)$] (blue). (b) The nonpolarizable model with the total and individual responses. (c) The total responses for the polarizable model (black), the nonpolarizable model (red), and the difference between them (green).

izable models. For the nonpolarizable model, the only contribution is $\langle \boldsymbol{J}(t)\cdot\boldsymbol{J}(0)\rangle_\omega$. For the polarizable model, there are three contributions, $\langle \boldsymbol{J}(t)\cdot\boldsymbol{J}(0)\rangle_\omega$, $\langle \boldsymbol{m}(t)\cdot\boldsymbol{m}(0)\rangle_\omega$, and $\langle \boldsymbol{J}(t)\cdot\boldsymbol{m}(0)\rangle_\omega$. $\langle \boldsymbol{J}(t)\cdot\boldsymbol{J}(0)\rangle_\omega$ contributes the most to the spectrum, while the latter two cross the whole spectrum. The cross-correlation $\langle \boldsymbol{J}(t)\cdot\boldsymbol{m}(0)\rangle_\omega$ enhances the intensity of the spectrum, which means the cross-correlation between the charge and the induced dipole moves toward the same direction as the system evolves in time. Although the direct correlation of the induced dipoles contributes moderately to the spectrum, the cross-correlation between charges and dipoles contributes more than one-third of the intensity to the spectrum, as found previously.[104] Thus, the inclusion of induced dipoles significantly enhances the conductivity spectrum.

The conductivity spectrum may be compared with the DOS for the center-of-masses of $EMIM^+$ and NO_3^- in Figure 9, as well as the DOS for H-atoms in Figure 3. The single-ion motion produces a relatively strong intensity in the conductivity spectrum. As can be seen from Figure 13, there is a broad band in the low frequency region, whose peak position is at ∼120 and ∼100 cm^{-1} for the polarizable and nonpolarizable models, respectively. In response to the single-ion motion, the induced dipoles, as well as their cross-correlation with the moving charges, also enhance the intensity of the conductivity spectrum,

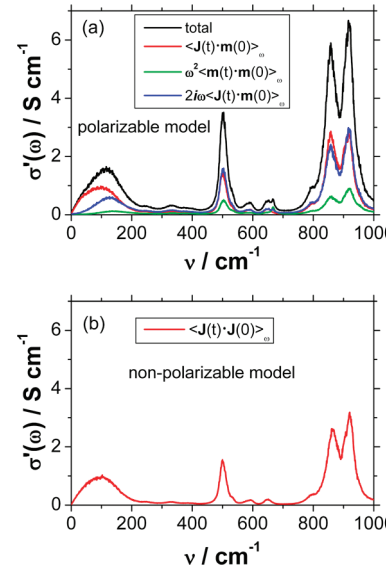

Figure 13. The real part of the conductivity spectrum for the polarizable model and the nonpolarizable model. (a) The polarizable model with the total spectrum (black) and the individual contributions from $\langle \boldsymbol{J}(t)\cdot\boldsymbol{J}(0)\rangle_\omega$ (red), $\omega^2\langle \boldsymbol{m}(t)\cdot\boldsymbol{m}(0)\rangle_\omega$, (green), and $i\omega\langle \boldsymbol{J}(t)\cdot\boldsymbol{m}(0)\rangle_\omega$ (blue). (b) The nonpolarizable model for which the only contribution is from $\langle \boldsymbol{J}(t)\cdot\boldsymbol{J}(0)\rangle_\omega$ (red).

as shown in Figure 13a. There are several bands in the H-atom DOS for both the polarizable and nonpolarizable models, as shown in Figure 3. For the band at ∼500 cm^{-1} in the conductivity spectrum, normal-mode analysis shows that this vibration can be attributed to the in-plane librational motions of the imidazolium ring of the $EMIM^+$ ion,[103] which involves all the ring H-atoms. Such motion interacts with the hydrogen bonding network and gives a relatively strong intensity, similar to the IR peak seen at ∼600 cm^{-1} in water.[106] The higher frequency bands peaked at ∼530 and ∼595 cm^{-1} in the H-atom DOS may be attributed to the bending motion of the imidazolium ring and are also captured in the conductivity spectrum. The bands at 790 and 950 cm^{-1}, which are related to H7-atoms twisting and C7−C8 stretching motions, make negligible contributions to the spectra.

The zero-frequency cases for eqs 16 and 17 give the Green-Kubo relation for the static (dc) conductivity $\sigma_0 = 1/(3k_BTV)\int_0^\infty dt\langle \boldsymbol{J}(t)\cdot\boldsymbol{J}(0)\rangle$.[81,107] Note that the contribution from the induced dipole, $\boldsymbol{m}$, vanishes at zero frequency for the polarizable model, because the static electrical conductivity is solely determined by the motion of individual ions. However, the presence of the polarizable sites can alter $\langle \boldsymbol{J}(t)\cdot\boldsymbol{J}(0)\rangle_\omega$ and thus contribute to σ_0 in an indirect way. Unfortunately, because of limited MD simulation time, the integrated σ_0 by the Green-Kubo relation is very difficult to fully converge. Therefore, for the IL system at room temperature, it is difficult to estimate σ_0 by the Green-Kubo relation from current 10 ns of equilibrium MD simulation data, as also reported by Urahata and Ribeiro with a united-atom model.[108] Madden and co-workers utilized the transverse conductivity spectrum with small k and ω to evaluate the static electrical conductivity,[104] similar to the method of estimating the shear viscosity (see the Appendix). This method is not further pursued here, but may be of interest to investigate in further studies. Alternatively, σ_0 may be estimated by the Einstein-Helfand relation with $\sigma_0 = 1/(6k_BTV)$ $\lim_{t\to\infty}$ $(d/dt)\langle\Delta M_J(t)^2\rangle$,[52] where $\langle\Delta M(t)^2\rangle = \langle|\boldsymbol{M}_J(t) - \boldsymbol{M}_J(0)|^2\rangle$ is the mean-square collective charge displacement, and $\boldsymbol{M}_J(t) - \boldsymbol{M}_J(0) = \int_0^t \boldsymbol{J}(t')dt'$. Note that $\boldsymbol{M}_J(t)$ by the above equation is different than the value given by the charge distribution at time

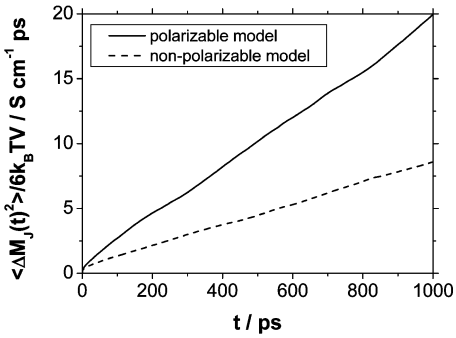

Figure 14. Conductivity estimated by the Einstein relation for the polarizable model (solid) and the nonpolarizable model (dashed). This figure shows the integration up to 1194 ps.

t,[49] that is, $\boldsymbol{M}_J(t) = \sum_{i=1}^{N_{atoms}} q_i \boldsymbol{r}_i(t)$. For the latter, the use of periodic boundary conditions complicates the definition as it varies discontinuously while ions leave one side of the simulation cell and re-enter from the other side.[104] Also note that $\boldsymbol{M}_J(0)$, that is, the total system dipole moment at time 0 due to charge distribution, cancels and does not come into the final expression.

Figure 14 shows the mean-square collective charge displacement. The direct conductivity σ_{dc}, estimated via the slope of $\langle \Delta M(t)^2 \rangle$, is 0.019 S/cm (molar conductivity $\Lambda_{E-H} = 2.78$ S cm^2/mol) and 0.0084 S/cm ($\Lambda_{E-H} = 1.35$ S cm^2/mol) for the polarizable and nonpolarizable models, respectively, which fall in the range of experimental measurements of slightly different ILs.[15,109] Since each individual trajectory runs for 10 ns, σ_{dc} may still not be well converged. However, a qualitative comparison can still be made. The dc conductivity of the polarizable model is about 2 times larger than that of the nonpolarizable model. This is consistent with the self-diffusion constants in Table 1, which shows that the polarizable model leads to about 2.5−3 times faster diffusion than that of the nonpolarizable model.

The electric conductivity can also be related to the diffusion constant as $\sigma_{dc} = (1/k_BT)(q_+^2\rho_+ D_+ + q_-^2\rho_- D_-)(1 - \Delta)$, where q, ρ, and D are the charge, number density, and self-diffusion constant for the cation and the anion,respectively, and Δ is a factor related to the cross-correlations between different charged particles.[81,110] Assuming that the term Δ is negligible, corresponding to the ideal Nernst−Einstein behavior, and utilizing the self-diffusion constants in Table 1 estimated by the Einstein relation, the computed dc conductivity is 0.030 S/cm ($\Lambda_{N-E} = 4.39$ S cm^2/mol) and 0.011 S/cm ($\Lambda_{N-E} = 1.77$ S cm^2/mol) for the polarizable and nonpolarizable models, respectively. Previous simulation demonstrated that oppositely charged ion pairs due to cross-correlation of different charged particles and the term $\Delta > 0$ deviating from ideal Nernst−Einstein behavior make the electric conductivity calculated by the ideal Nernst−Einstein equation the upper bound.[11] Specifically, $\Delta \approx 0.37$ and 0.24, respectively, for the polarizable and nonpolarizable models. Therefore, ion association and local cluster formation is important in this IL even at 400 K. In addition, the degree of ion association is larger for the polarizable model, and such behavior is consistent with stronger spatial heterogeneity, estimated via heterogeneity order parameters (HOPs) in the accompanying paper.[10]

The frequency-dependent dielectric constant $\varepsilon(\omega)$ is related to $\sigma(\omega)$ by $\Sigma(\omega) = \varepsilon(\omega) - 1 + i4\pi\sigma(\omega)/\omega$,[48,49,82,104] in which $\Sigma(\omega)$ is the generalized dielectric constant accessible experimentally, $\sigma(\omega)$ is the contribution from conductivity, as given by eq 16 for the nonpolarizable model and eq 17 for the polarizable model, respectively. Rich amounts of information may be obtained via detailed dielectric response, which for the polarizable model includes the cross-correlation between the molecular dipole, the induced dipole, and the current as well as the approximate molecular dipoles for the reorientational contribution. Detailed dielectric study, which separates the contribution of translational, rotational, and induced dipole moments, as well as cross-correlations among them, deserves further investigation. One point to note, however, is that, for the polarizable model, the contribution from $\langle m^2 \rangle$ in eq 17 denotes the instantaneous electronic response and thus gives the high frequency optical dielectric constant, that is, $\varepsilon_\infty = 1 + (4\pi\langle m^2 \rangle)/(3k_BTV) = 3.35$, which is in good agreement with experimental measurement, fitted by the multiterm Debye model, for slightly different ILs.[15,46,54] Therefore, the polarizable model utilized in this study produces reasonable ε_∞.

III.6. Correlation between Electrostatic Energy and Polarization Energy. In this section, we analyze the electrostatic energy by the charge−charge interactions and the induction energy by the charge-dipole interactions, by inserting a probe ion into the IL bulk system, stimulated by the study of Kato et al.[80] The average electrostatic energy on the probe ion i, caused by the charge−charge interactions with charge j, is given by $u_q = \langle \sum_{j \neq i} q_i q_j / r_{ji} \rangle$. The average induction energy on the probe ion i, caused by the charge-dipole interactions with dipole j, is given by $u_\mu = \langle -\sum_{j \neq i} \mu_j \cdot \boldsymbol{e}_j \rangle$, in which $\boldsymbol{e}_j = q_i \boldsymbol{r}_{ji}/r_{ji}^3$ is the electric field on j caused by the charge q_i. Note that there is no dipole−dipole interactions between the probe ion and IL, since the probe ion is nonpolarizable. Since dipole−dipole interactions is proportional to $1/r^3$, the contribution is of tertiary compared to charge−charge and charge-dipole interactions. u_q and u_μ are calculated by Ewald summation[100,111] during simulation.

Figure 15 shows the two-dimensional distribution of u_q versus u_μ of the probe ion, which was obtained by averaging the 2 ns simulations of a nonpolarizable probe ion (of charge +1e and −1e) in the polarizable IL model. It can be seen that the overall electrostatic energy is lower for the positive probe ion than the negative one. This may be attributed to the smaller size of the IL anion NO_3^-, as compared to the bulky IL cation $EMIM^+$, on which the charge is sparsely distributed. NO_3^- can have a closer contact with the positive probe ion, which is stabilized by lower electrostatic energy. However, the low electrostatic energy is compensated by the relative higher induction energy. Though the overall trend of u_μ is to lower the electrostatic energy, it can be seen that u_μ works against u_q, and even becomes positive at very low u_q. The above observation, together with the negative slope for the distribution of u_q versus u_μ is in good agreement with the study by Kato et al. using a CRK model.[80] The slope is approximately −0.5 for both the probe ion of +1e and −1e charges, which means that two configurations of energy difference −10 kcal/mol by charge interactions becomes −5 kcal/mol upon dipole interactions added. Therefore, the induction energy tends to be anticorrelated with the electrostatic energy by the permanent charges, and the net result is that energy barrier is effectively lowered for an ion moving from one basin to the other. The above analyses demonstrate that ionic motion is accelerated by the polarization effects. The origin of such anticorrelation between u_q and u_μ is of interest to pursue in further study.

IV. Summary

In the current study, a second generation of a polarizable model for the IL $EMIM^+/NO_3^-$ was developed, and the dynamical properties for both the polarizable and nonpolarizable models were compared. The comparison of the structural properties was reported in the accompanying paper.[10] For the

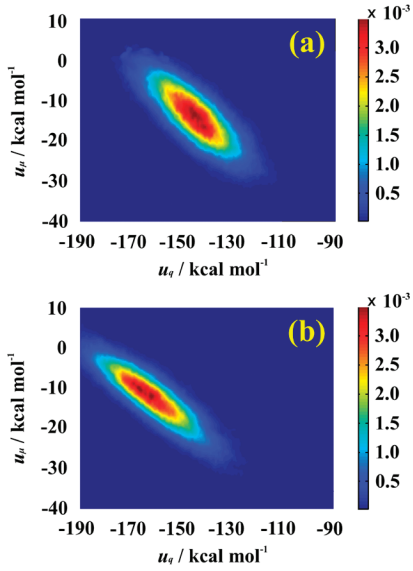

Figure 15. Two-dimensional statistical distribution of the electrostatic energy by the permanent charge interaction, u_q, vs the induction energy, u_μ, of a probe ion of partial charge −1e (a), and +1e (b).

dynamical properties investigated in this paper, the polarizable model always shows faster relaxation, including translational and reorientational motions, than the nonpolarizable model. Thus, the polarizable model gives higher self-diffusion coefficients, ionic conductivity, and lower shear viscosity than the polarizable counterpart. The analysis shows that the polarization energy caused by induction is anticorrelated with the electrostatic interactions by the permanent charges, and the net result is that the energy barrier is effectively lowered for an ion to move from one basin to the other. Therefore, the ionic motion is accelerated by the polarization effect. Such enhancement of the ionic mobility due to the polarization effect was also nicely explained by Hansen and McDonald.[81] For the nonpolarizable model, the local charge neutrality around a diffusing ion can only be maintained by the displacement of its neighbors; when polarization is allowed, an additional screening mechanism is present that does not require the movement of the ions. The net result is that the cage effect is smaller for the polarizable ions, which may bring simulation results with the polarizable model in better agreement with experimental measurements.[81]

Nevertheless, both models exhibit slow dynamics, characterized by two-step relaxation besides the fast initial collision in cage. Both models show certain properties that are similar to a supercooled liquid behavior, even though the simulations were run at 400 K, which is 89 K above the melting point of $EMIM^+/NO_3^-$. The structural relaxations, that is, ionic MSDs and transverse current correlation functions, are well modeled by a memory function, with a fast Gaussian initial relaxation followed by the two-step exponential functions for β- and α- structural relaxations. The self-part of the van Hove functions strongly deviate from ideal Gaussian behavior and thus highlight the dynamical heterogeneity in ILs. On the other hand, the distinct part of the van Hove function does not show apparent trend of cation−anion association for both the nonpolarizable and the polarizable models. Apart from the overall slow dynamics, the relaxation of the H-atoms attached to the methyl-group demonstrates a fast initial relaxation, which is attributed to the "free-rotor" type of motion. Also, the ethyl-group shows the fastest overall relaxation, probably due to the spatial heterogeneity from the separation of the polar and nonpolar regions. Thus, the nonpolar ethyl side-group relaxes fast due to the weak electrostatic interactions. Such flexibility may enhance the entropic effect and favor the liquid state at room temperature.

For the polarizable model, the contribution from the charge−dipole cross-correlation and dipole−dipole autocorrelation is found to enhance the conductivity spectrum across the whole frequency range. The hydrogen-bonding dynamics produce high intensity in the conductivity spectrum. The additional charge−dipole and dipole−dipole interactions enhance the intermolecular interactions, as evidenced by the red shift of the intramolecular C−H stretch modes. Furthermore, the degree of ion association is larger for the polarizable model, and such behavior is consistent with the stronger spatial heterogeneity, which is highlighted by the heterogeneity order parameters (HOPs) described in the accompanying paper.[10] Therefore, ion association and local cluster formation is significant in this IL even at 400 K.

On the basis of the above discussion, the electronic polarization effect is two-faced. On one hand, the polarizable forcefield results in faster relaxation due to the induction effect which effectively screens the electrostatic interactions, and simulation based on the polarizable model may be analogous to simulation at higher temperatures with the nonpolarizable model. On the other hand, the enhanced short-range intermolecular interactions due to the additional charge-dipole and dipole−dipole interactions for the polarizable model result in a higher degree of ion association. Such combination of enhanced short-range electrostatic interaction and attenuated long-range electrostatic interaction, introduced by the polarization effect, may challenge the validity of using a nonpolarizable forcefield, which balances these two features.

The major shortcoming of the polarizable model is that it requires much more computational resources than the nonpolarizable model, due to the additional long-range charge-dipole and dipole−dipole interactions introduced by the polarization effect. A recently developed multiscale coarse-graining methodology[112] was successfully applied to ILs,[113] which reproduces very well the structural properties given by the all-atom polarizable model and may be promising for simulating complex IL systems over much larger spatial scales with a reasonable amount of computational expense.

Acknowledgment. This study is supported by NFSC (No. 20503013, 20873068) and the 973 Program (2009CB220100) of China. This work cannot be done without the continuous encouragement and support from Dr. Gregory A. Voth. The authors thank Dr. Christian J. Burnham and Dr. Jonggu Jeon for helpful discussions. We are also grateful to Mr. Zhen Cao's help on preparing Figure 15. The allocations of supercomputing time at the Center for High Performance Computing (CHPC) at the University of Utah and Institute of Scientific Computing (NKstars HPC program) at Nankai University are gratefully acknowledged.

Appendix

Estimating Shear Viscosity by Transverse Current Correlation Function. Because of the difficulty of obtaining the shear viscosity by the Green-Kubo method utilizing the stress tensor correlation function, we adopt an alternative method to estimate it by fitting the transverse current correlation function with a memory function kernel reported in our previous study.[72] The memory function, which is more general than the correlation function, should take a simple form. Ailawadi, Rahman, and Zwanzig[114] proposed and tested the exponential and Gaussian memory functions in their study of the viscosity of liquid argon

TABLE A.1: The Fitted Parameters for $C_t(k,\omega)$ with $k = 0.014$ Å^{-1} and the Shear Viscosity, Using the Memory Function Given in Equation 5

	ω_t^2 (ps^{-2})[a]	β_k	α_k	τ_{1k} (ps)	$\tau_{\beta k}$ (ps)	$\tau_{\alpha k}$ (ps)	$\eta(k)$ (c.p.)[b]	η (c.p.)[c]
polarizable model	15.721	6.911×10^{-2}	5.040×10^{-2}	3.720×10^{-2}	0.687	9.972	7.54	18.03
	ω_t^2 (ps^{-2})[a]	β_k	α_k	τ_{1k} (ps)	$\tau_{\beta k}$ (ps)	$\tau_{\alpha k}$ (ps)	$\eta(k)$ (c.p.)[b]	η (c.p.)[c]
nonpolarizable model	19.578	6.937×10^{-2}	3.984×10^{-2}	3.039×10^{-2}	0.755	12.720	11.65	47.42

[a] $\omega_t^2 = \langle|\dot{\boldsymbol{J}}_t(k,t)|^2\rangle/\langle|\boldsymbol{J}_t(k,0)|^2\rangle$ is calculated by taking the numerical derivatives of the MD simulation data. [b] Wave-vector dependent shear viscosity calculated by eq A.1 using the fitted parameters in this table. [c] Shear viscosity estimated by the Stokes−Einstein relation, eq A.4, with the self-diffusion coefficient of the cations listed in Table 1.

and found that the Gaussian function gives the best fit. Levesque, Verlet, and Kürkijarvi[115] proposed a two-step exponential decay function in their study of Lennard-Jones fluids. The same function was also used by Balucani, Pasqualini, and co-workers in their study of the shear viscosity of HCl.[116] Here, we adopt the three-step memory function $M_t(k,t)$, defined in eq 5, to replace the two-step memory function proposed in our previous study.[72]

We follow the method described in our previous study,[72] which employs the transverse current correlation function $C_t(k,t) = \langle \boldsymbol{J}_t(\boldsymbol{k},t)\cdot\boldsymbol{J}_t(-\boldsymbol{k},0)\rangle$, where $\boldsymbol{J}_t(\boldsymbol{k},t) = (1)/(N)^{1/2}\sum_{i=1}^{N}\hat{\boldsymbol{k}} \times m_i\boldsymbol{v}_i(t)\exp[i\boldsymbol{k}\boldsymbol{r}_i(t)]$ is the transverse current, m_i, $\boldsymbol{v}_i$, and $\boldsymbol{r}_i$ are the mass, center-of-mass velocity, and position of the ith ion, respectively. Wave vectors of the same magnitude are averaged over in the calculation of $C_t(k,t)$. By utilizing the memory function approach given by $dC_t(k,t)/dt = -\int_0^t dt'\, M_t(k,t-t')C_t(k,t')$, the wave-vector dependent shear viscosity is given by[81,90]

$$\eta(k) = \lim_{\omega\to 0}\frac{\rho}{k^2}\tilde{M}_t(k,\omega) = \frac{\rho}{k^2}\tilde{M}_t(k,0) \qquad \text{(A.1)}$$

where $\tilde{M}_t(k,0)$ is given by eq 9, and $\tilde{M}_t(k,\omega)$ is the Laplace transform of eq 5 with $s = i\omega$. $M_t(k,t)$ may be obtained by fitting the transverse current correlation function $C_t(k,t)$, or its spectrum $C_t(k,\omega)$, so that

$$C_t(k,\omega) = \frac{2M_t'(k,\omega)}{[\omega - M_t''(k,\omega)]^2 + M_t'(k,\omega)^2} \qquad \text{(A.2)}$$

In the above equation, $M_t'(k,\omega) = \int_0^\infty dt\, \cos\omega t M_t(k,t)$ and $M_t''(k,\omega) = \int_0^\infty dt\, \sin\omega t M_t(k,t)$ are the real and imaginary parts of the Laplace transform of $M_t(k,t)$, respectively, which are further expressed as

$$M_t'(k,\omega) = \omega_t^2\left[(1-\alpha_k-\beta_k)\tau_{1k}\exp(-\tau_{1k}^2\omega^2/\pi) + \frac{\alpha_k/\tau_{2k}}{\omega^2+1/\tau_{2k}^2} + \frac{\beta_k/\tau_{3k}}{\omega^2+1/\tau_{3k}^2}\right]$$

$$M_t''(k,\omega) = \omega_t^2\left[(1-\alpha_k-\beta_k)\tau_{1k}\exp(-\tau_{1k}^2\omega^2/\pi)\times \mathrm{erfi}(\tau_{1k}\omega/\pi^{1/2}) + \frac{\alpha_k\omega}{\omega^2+1/\tau_{2k}^2} + \frac{\beta_k\omega}{\omega^2+1/\tau_{3k}^2}\right] \qquad \text{(A.3)}$$

where $\mathrm{erfi}(\tau_{1k}\omega/\pi^{1/2}) = \mathrm{erf}(i\tau_{1k}\omega/\pi^{1/2})/i = (2/\pi^{1/2})\int_0^{\tau_{1k}\omega/\pi^{1/2}}\exp(y^2)dy$ is the imaginary error function and $\exp(-\tau_{1k}^2\omega^2/\pi)\int_0^{\tau_{1k}\omega/\pi^{1/2}}\exp(y^2)dy$ is Dawson's integral.[117]

The factor 2 on the right-hand side of eq A.2 accounts for the one-side Laplace transform. Extrapolation of eq A.1 to the $k\to 0$ limit gives the hydrodynamic value of shear viscosity. Here, we further approximate the hydrodynamic (long time, long distance) shear viscosity by the wave-vector dependent shear viscosity at $k = 2\pi/L(1,0,0) = 0.14$ Å^{-1}. Similar approximation has been used by Madden and co-workers for estimating the static electric conductivity.[104] If $C_t(k,\omega)$ is fully converged, the zero frequency value wave-vector dependent shear viscosity may be directly evaluated by $\eta(k) = (\rho/k^2)(1/C_t(k,\omega=0))$, where $C_t(k,\omega=0) = \int_0^\infty dt\, \cos\omega t C_t(k,t)$. This method has been used by Urahata and Ribeiro to estimate shear viscosity for other ILs.[108,118]

Figure 16 shows the normalized transverse current correlation function $C_t(k,t)$ (insets), as well as $C_t(k,\omega)$ and its fit by eq 11, for both the polarizable and nonpolarizable models. The wave vector $k = 2\pi/L(1,0,0) = 0.14$ Å^{-1} with $L\sim 46$ Å side length of the cubic simulation box is the smallest wave vector in the current simulation. It can be seen that the three-step memory function, given by eq 5, fits $C_t(k,\omega)$ reasonably well and the inverse cosine transform to the time frame is also in good agreement with $C_t(k,t)$. The fitting parameters, as well as the wave vector dependent shear viscosity $\eta(k)$ given by eq A.1 at $k = 0.14$ Å^{-1}, are also shown in Table A.1 It can be seen that the initial ultrafast relaxation time τ_1 in the 10^{-2} ps range is similar for both the polarizable and nonpolarizable models, indicating that the initial ultrafast relaxation, when the ions explore the local potential energy basin, occurs in a similar time scale for both models. The relaxation times τ_β and τ_α, characterizing the two-step structural relaxations for the polarizable model, are shorter than those for the nonpolarizable model, indicating that the polarizable model has a faster relaxation. Since $k = 0.14$ Å^{-1} represents the smallest wave vector for our system, we adopt $\eta(k)$ calculated by eq A.1, using the fitted parameters listed in Table A.1, as an approximation to the hydrodynamic (long time, low wave-vector) shear viscosity, which is 7.54 c.p. and 11.65 c.p. for the polarizable and nonpolarizable models, respectively. Using $\eta(k)$ with $k = 2\pi/L(1,1,0) = 0.19$ Å^{-1} gives similar results.

Seddon and co-workers[119] measured the viscosity of $EMIM^+/NO_3^-$ and fitted the Vogel−Fülcher−Tammann (VFT) empirical equation of viscosity versus absolute temperature by $\ln(\eta) = k/(T - T_0) + 1/2\ln(T) + \ln(A)$, with $k = 1447$ K, $T_0 = 113.6$ K, and $\ln(A) = -6.5624$. By feeding the viscosity value calculated by eq A.1 into the above relation, one can estimate that the simulation with the polarizable model corresponds to an experimental temperature of ∼370 K and the simulation with the nonpolarizable model corresponds to an experimental temperature of ∼351 K. Therefore, although the MD simulation is performed at 400 K for both the polarizable and the nonpolarizable models, they behave as if they were run at lower temperatures, with the polarizable model ∼30 K below and the nonpolarizable model ∼49 K below the experimental temperature of 400 K. Considering the melting

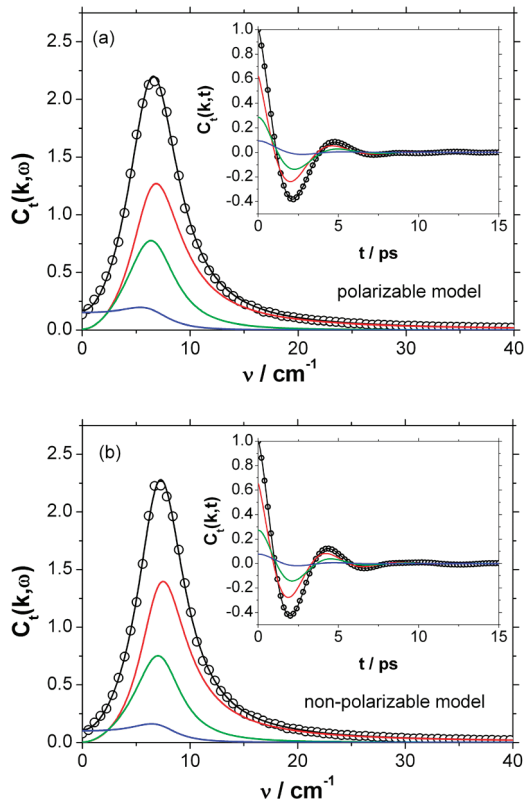

Figure 16. Fourier transform of the normalized transverse current correlation function $C_t(k,\omega)$ obtained from the MD simulations as well as from the fit by eq A.2, for the polarizable model (a) and the nonpolarizable model (b), respectively. The open circles are the discrete Fourier transform of $C_t(k,t)$ from the MD simulation data. The solid line is the fitted $C_t(k,\omega)$ by eq A.2, with the total (black) and the individual contributions from the fast Gaussian decay (red), β-relaxation (green), and α-relaxation (blue) in eq 5, individually. The insets show $C_t(k,t)$ from the MD simulation data and from the fit with eq A.2 using the memory function defined in eq 5.

point of $EMIM^+/NO_3^-$ at ~311 K, the effective temperature is ~40 K and ~59 K above the melting point, respectively, for the nonpolarizable and the polarizable models. It is of interest to note that the polarizable model, although it is effectively ~59 K higher than the melting point, still exhibits supercooled behavior, characterized by the β- and α-relaxations in the incoherent intermediate scattering function $F_s(k,t)$. Thus, supercooled behavior may be one of the fundamental properties associated with ILs even at considerably higher temperatures than the melting point. Triolo and coworkers performed a quasielastic neutron experiment on $BMIM^+/PF_6^-$ and also found supercooled behavior at 320 K,[27] which is about 40 K higher than the melting point of $BMIM^+/PF_6^-$ at ~280 K.

The hydrodynamic shear viscosity and diffusion constant is related via Stokes−Einstein (SE) relation, that is[81]

$$\eta = \frac{k_B T}{c\pi D a} \qquad \text{(A.4)}$$

where c is 6 for stick boundary condition or is 4 for slip boundary condition, and a can be interpreted as the hydrodynamic radius of the diffusing ion in the system. The use of slip boundary general leads to good estimation of molecular radius.[81] Watanabe and co-workers adopted the van der Waals radius of $EMIM^+$ of 3.03 Å and estimated that $c = 2.9$ for $EMIM^+/TFSI^-$ via the slope of $D - \eta$ relation at different temperature.[24] Alternatively, once a is known, eq A.4 may be used for a rough estimation of the shear viscosity. Here, we use self-diffusion coefficient of the cation in Table 1, and the van der Waals radius of $EMIM^+$ 3.03 Å,[24] and $c = 4.0$, and obtain the shear viscosity 18.03 c.p. for the polarizable model and 47.42 c.p. for the nonpolarizable model. It is notable that the shear viscosities by SE relation are 2.4 and 4.1 times larger than the viscosities obtained by eq A.1, respectively, for the polarizable and nonpolarizable models, as listed in Table A.1. The difference for the shear viscosity estimated by eq A.1 and eq A.4 may be sealed by increasing the hydrodynamic radius a. In a study on the Li/KCl eutectic inorganic molten salt, Madden and coworks showed that the hydrodynamic radius with slip boundary condition, $c = 4$ in eq A.4, is considerably larger than the bare ionic radius.[120] Recently, Ludwig and co-workers systematically studied the relation between viscosity and diffusion coefficient ILs and found that SE relation can not be applied to such a system with highly dynamical heterogeneity.[121]

It should also be emphasized that the shear viscosity estimated in this study is higher than the previously reported results, especially for the nonpolarizable model.[72] The three-step memory function kernel, given in eq 5, may give a larger viscosity compared to the two-step memory kernel used in our previous study because the long time memory accounts for higher friction and thus larger viscosity. In equilibrium MD simulations, long time simulation is needed to get fully converged dynamical properties. Because of the slow dynamics of room temperature IL systems, the current simulation time of 10 ns may still not be long enough to compute the fully converged dynamical properties, especially for the nonpolarizable model, to permit a quantitative comparison with experimental values. At this point, estimating shear viscosity with nonequilibrium MD (NEMD)[19,55,122] may be an alternative choice. Interestingly, a recent study on $EMIM^+/TFSI^-$ using a polarizable model shows that the viscosity, estimated by Einstein relation with both the diagonal and off-diagonal stress tensor in an equilibrium MD, is essentially the same as the viscosity estimated by NEMD simulation.[76,123] This method may be adopted in an equilibrium MD simulation to estimate viscosity due to its accuracy as well as relatively less demand on the computational resource.

Supporting Information Available: Figure S1 compares the MSDs of the polarizable model with both the iteration method and the ext-L method for the dipole degrees of freedom, and the nonpolarizable model. This material is available free of charge via the Internet at http://pubs.acs.org.

References and Notes

(1) Canongia Lopes, J. N.; Shimizu, K.; Pádua, A. A. H.; Umebayashi, Y.; Fukuda, S.; Fujii, K.; Ishiguro, S.-i. *J. Phys. Chem. B* **2008**, *112*, 1465.

(2) (a) Krossing, I.; Slattery, J. M.; Daguenet, C.; Dyson, P. J.; Oleinikova, A.; Weingärtner, H, *J. Am. Chem. Soc.* **2006**, *128*, 13427. (b) Inamura, Y.; Yamamuro, O.; Hayashi, S.; Hamaguchi, H. *Physica B* **2006**, *385−386*, 732.

(3) Xiao, D.; Hines, L. G., Jr; Li, S.; Bartsch, R. A.; Quitevis, E. L.; Russina, O.; Triolo, A. *J. Phys. Chem. B* **2009**, *113*, 6426.

(4) (a) Welton, T. *Chem. Rev.* **1999**, *99*, 2071. (b) Wasserscheid, P.; Keim, W. *Angew. Chem., Int. Ed.* **2000**, *39*, 3772. (c) Pârvulescu, V. I.; Hardacre, C. *Chem. Rev.* **2007**, *107*, 2615. (d) van Rantwijk, F.; Sheldon, R. A. *Chem. Rev.* **2007**, *107*, 2757. (e) El Seoud, O. A.; Koschella, A.; Fidale, L. C.; Dorn, S.; Heinze, T. *Biomacromolecules* **2007**, *8*, 2629. (f) Haumann, M.; Riisager, A. *Chem. Rev.* **2008**, *108*, 1474. (g) Greaves, T. L.; Drummond, C. J. *Chem. Rev.* **2008**, *108*, 206.

(5) Castner, E. W., Jr.; Wishart, J. F. *J. Chem. Phys.* **2010**, *132*, 120901.

(6) Rogers, R. D.; Voth, G. A. *Acc. Chem. Res.* **2007**, *40*, 1077.

(7) (a) Katayanagi, H.; Hayashi, S.; Hamaguchi, H.; Nishikawa, K. *Chem. Phys. Lett.* **2004**, *392*, 460. (b) Tokuda, H.; Tsuzuki, S.; Susan, M. A. B. H.; Hayamizu, K.; Watanabe, M. *J. Phys. Chem. B* **2006**, *110*, 19593.

(8) Triolo, A.; Mandanici, A.; Russina, O.; Rodriguez-Mora, V.; Cutroni, M.; Hardacre, C.; Nieuwenhuyzen, M.; Bleif, H.-J.; Keller, L.; Ramos, M. A. *J. Phys. Chem. B* **2006**, *110*, 21357.

(9) Heimer, N. E.; Wilkes, J. S.; Wahlbeck, P. G.; Carper, W. R. *J. Phys. Chem. A* **2006**, *110*, 868.

(10) Yan, T.; Wang, Y.; Knox, C. *J. Phys. Chem. B,* [Online early release]. DOI:10.1021/jp9089112.

(11) Del Pópolo, M. G.; Voth, G. A. *J. Phys. Chem. B* **2004**, *108*, 1744.

(12) (a) Hu, Z.; Margulis, C. J. *Proc. Natl. Acad. Sci. U.S.A.* **2006**, *103*, 831. (b) Hu, Z.; Margulis, C. J. *Acc. Chem. Res.* **2007**, *40*, 1097. Habasaki, J.; Ngai, K. L. *J. Chem. Phys.* **2008**, *129*, 194501.

(13) Cadena, C.; Zhao, Q.; Snurr, R. Q.; Maginn, E. J. *J. Phys. Chem. B* **2006**, *110*, 2821.

(14) Triolo, A.; Russina, O.; Hardacre, C.; Nieuwenhuyzen, M.; Gonzalez, M. A.; Grimm, H. *J. Phys. Chem. B* **2005**, *109*, 22061.

(15) Weingärtner, H.; Knocks, A.; Schrader, W.; Kaatze, U. *J. Phys. Chem. A* **2001**, *105*, 8646.

(16) Daguenet, C.; Dyson, P. J.; Krossing, I.; Oleinikova, A.; Slattery, J.; Wakai, C.; Weingärtner, H. *J. Phys. Chem. B* **2006**, *110*, 12682.

(17) Weingärtner, H.; Sasisanker, P.; Daguenet, C.; Dyson, P. J.; Krossing, I.; Slattery, J. M.; Schubert, T. *J. Phys. Chem. B* **2007**, *111*, 4775.

(18) Borodin, O.; Smith, G. D. *J. Phys. Chem. B* **2006**, *110*, 11481.

(19) Kelkar, M. S.; Maginn, E. J. *J. Phys. Chem. B* **2007**, *111*, 4867.

(20) Shim, Y.; Jeong, D.; Manjari, S.; Choi, M. Y.; Kim, H. J. *Acc. Chem. Res.* **2007**, *40*, 1130.

(21) Shim, Y.; Kim, H. J. *J. Phys. Chem. B* **2008**, *112*, 11028.

(22) (a) Every, H. A.; Bishop, A. G.; MacFarlane, D. R.; Orädd, G.; Forsyth, M. *Phys. Chem. Chem. Phys.* **2004**, *6*, 1758. (b) Tokuda, H.; Ishii, K.; Susan, M. A. B. H.; Tsuzuki, S.; Hayamizu, K.; Watanabe, M. *J. Phys. Chem. B* **2006**, *110*, 2833. (c) Lacob, C.; Sangoro, J. R.; Serghei, A.; Naumov, S.; Kärger, J.; Friedrich, C.; Kremer, F. *J. Chem. Phys.* **2008**, *129*, 234511.

(23) Tokuda, H.; Hayamizu, K.; Ishii, K.; Susan, M. A. B. H.; Watanabe, M. *J. Phys. Chem. B* **2004**, *108*, 16593.

(24) Tokuda, H.; Hayamizu, K.; Ishii, K.; Susan, M. A. B. H.; Watanabe, M. *J. Phys. Chem. B* **2005**, *109*, 6103.

(25) Rivera, A.; Brodin, A.; Pugachev, A.; Rössler, E. A. *J. Chem. Phys.* **2007**, *126*, 114503.

(26) Wulf, A.; Ludwig, R.; Sasisanker, P.; Weingärtner, H. *Chem. Phys. Lett.* **2007**, *439*, 323.

(27) Triolo, A.; Russina, O.; Arrighi, V.; Juranyi, F.; Janssen, S.; Gordon, M. S. *J. Chem. Phys.* **2003**, *119*, 8549.

(28) Pajzderska, A.; Gonzalez, M. A.; Wasicki, J. *J. Chem. Phys.* **2008**, *128*, 084507.

(29) Kuang, Q.; Zhang, J.; Wang, Z. *J. Phys. Chem. B* **2007**, *111*, 9858.

(30) Qiao, B.; Krekeler, C.; Berger, R.; Site, L. D.; Holm, C. *J. Phys. Chem. B* **2008**, *112*, 1743.

(31) Morrow, T. I.; Maginn, E. J. *J. Phys. Chem. B* **2002**, *106*, 12807.

(32) Cho, M.; Du, M.; Scherer, N. F.; Fleming, G. R. *J. Chem. Phys.* **1993**, *99*, 2410.

(33) Hyun, B.-R.; Dzyuba, S. V.; Bartsch, R. A.; Quitevis, E. L. *J. Phys. Chem. A* **2002**, *106*, 7579.

(34) Giraud, G.; Gordon, C. M.; Dunkin, I. R.; Wynne, K. *J. Chem. Phys.* **2003**, *119*, 464.

(35) Cang, H.; Li, J.; Fayer, M. D. *J. Chem. Phys.* **2003**, *119*, 13017.

(36) (a) Rajian, J. R.; S., L.; Bartsch, R. A.; Quitevis, E. L. *Chem. Phys. Lett.* **2004**, *393*, 372. (b) Shirota, H.; Funston, A. M.; Wishart, J. F.; Castner, E. W., Jr. *J. Chem. Phys.* **2005**, *122*, 184512. (c) Li, J.; Wang, I.; Fruchey, K.; Fayer, M. D. *J. Phys. Chem. A* **2006**, *110*, 10384.

(37) Xiao, D.; Rajian, J. R.; Li, S.; Bartsch, R. A.; Quitevis, E. L. *J. Phys. Chem. B* **2006**, *110*, 16174.

(38) Shirota, H.; Castner, E. W., Jr. *J. Phys. Chem. A* **2005**, *109*, 9388.

(39) Shirota, H.; Castner, E. W., Jr. *J. Phys. Chem. B* **2005**, *109*, 21576.

(40) Urahata, S. M.; Ribeiro, M. C. C. *J. Chem. Phys.* **2005**, *122*, 024511.

(41) Ribeiro, M. C. C. *J. Phys. Chem. B* **2007**, *111*, 5008.

(42) Hu, Z.; Huang, X.; Annapureddy, H. V. R.; Margulis, C. J. *J. Phys. Chem. B* **2008**, *112*, 7837.

(43) Shirota, H.; Nishikawa, K.; Ishida, T. *J. Phys. Chem. B* **2009**, *113*, 9831.

(44) Ishida, T.; Shirota, H.; Nishikawa, K. *J. Phys. Chem. B* **2009**, *113*, 9840.

(45) Schrödle, S.; Annat, G.; MacFarlane, D. R.; Forsyth, M.; Buchner, R.; Hefter, G. *Chem. Comm.* **2006**, 1748.

(46) Asaki, M. L. T.; Redondo, A.; Zawodzinski, T. A.; Taylor, A. J. *J. Chem. Phys.* **2002**, *116*, 10377.

(47) Caillol, J. M.; Levesque, D.; Weis, J. J. *J. Chem. Phys.* **1986**, *85*, 6645.

(48) Caillol, J. M.; Levesque, D.; Weis, J. J. *J. Chem. Phys.* **1989**, *91*, 5544.

(49) Caillol, J. M.; Levesque, D.; Weis, J. J. *J. Chem. Phys.* **1989**, *91*, 5555.

(50) Wakai, C.; Oleinikova, A.; Ott, M.; Weingärtner, H. *J. Phys. Chem. B* **2005**, *109*, 17028.

(51) (a) Schröder, C.; Rudas, T.; Steinhauser, O. *J. Chem. Phys.* **2006**, *125*, 244506. (b) Schröder, C.; Wakai, C.; Weingärtner, H.; Steinhauser, O. *J. Chem. Phys.* **2007**, *126*, 084511. (c) Schröder, C.; Rudas, T.; Neumayr, G.; Gansterer, W.; Steinhauser, O. *J. Chem. Phys.* **2007**, *127*, 044505. (d) Schröder, C.; Steinhauser, O. *J. Chem. Phys.* **2009**, *131*, 114504.

(52) Schröder, C.; Haberier, M.; Steinhauser, O. *J. Chem. Phys.* **2008**, *128*, 134501.

(53) Hunger, J.; Stoppa, A.; Schrödle, S.; Hefter, G.; Buchner, R. *ChemPhysChem* **2009**, *10*, 723.

(54) Stoppa, A.; Hunger, J.; Buchner, R.; Hefter, G.; Thoman, A.; Helm, H. *J. Phys. Chem. B* **2008**, *112*, 4854.

(55) Hu, Z.; Margulis, C. J. *J. Phys. Chem. B* **2007**, *111*, 4705.

(56) Maginn, E. J. *Acc. Chem. Res.* **2007**, *40*, 1200.

(57) Kowsari, M. H.; Alavi, S.; Ashrafizaadeh, M.; Najafi, B. *J. Chem. Phys.* **2008**, *129*, 224508.

(58) Lynden-Bell, R. M.; Del Pópolo, M. G.; Youngs, T. G. A.; Kohanoff, J.; Hanke, C. G.; Harper, J. B.; Pinilla, C. C. *Acc. Chem. Res.* **2007**, *40*, 1138.

(59) (a) Bhargava, B. L.; Balasubramanian, S. *J. Chem. Phys.* **2005**, *123*, 144505. (b) Siqueira, L. J. A.; Ribeiro, M. C. C. *J. Phys. Chem. B* **2007**, *111*, 11776. (c) Rey-Castro, C.; Vega, L. F. *J. Phys. Chem. B* **2006**, *110*, 14426. (d) Bagno, A.; D'Amico, F.; Saielli, G. *J. Mol. Liquid* **2007**, *131*−*132*, 17. (e) Kelkar, M. S.; Shi, W.; Maginn, E. J. *Ind. Eng. Chem. Res.* **2008**, *47*, 9115. (f) Tsuzuki, S.; Shinoda, W.; Saito, H.; Mikami, M.; Tokuda, H.; Watanabe, M. *J. Phys. Chem. B* **2009**, *113*, 10641. (g) Kowsari, M. H.; Alavi, S.; Ashrafizaadeh, M.; Najafi, B. *J. Chem. Phys.* **2009**, *130*, 014703.

(60) Dommert, F.; Schmidt, J.; Qiao, B.; Zhao, Y.; Krekeler, C.; Site, L. D.; Berger, R.; Holm, C. *J. Chem. Phys.* **2008**, *129*, 224501.

(61) (a) Canongia Lopes, J. N.; Pádua, A. A. H. *J. Phys. Chem. B* **2006**, *110*, 19586. (b) Canongia Lopes, J. N.; Pádua, A. A. H. *J. Phys. Chem. B* **2004**, *108*, 16893.

(62) (a) Canongia Lopes, J. N.; Deschamps, J.; Pádua, A. A. H. *J. Phys. Chem. B* **2004**, *108*, 2038. (b) Canongia Lopes, J. N.; Deschamps, J.; H., P. A. A. *J. Phys. Chem. B* **2004**, *108*, 11250.

(63) Liu, Z.; Huang, S.; Wang, W. *J. Phys. Chem. B* **2004**, *108*, 12978.

(64) Logotheti, G.; Ramos, J.; Economou, I. G. *J. Phys. Chem. B* **2009**, *113*, 7211.

(65) Bhargava, B. L.; Balasubramanian, S. *J. Chem. Phys.* **2007**, *127*, 114510.

(66) Shim, Y.; Duan, J.; Choi, M. Y.; Kim, H. J. *J. Chem. Phys.* **2003**, *119*, 6411.

(67) Micaelo, N. M.; Baptista, A. M.; Soares, C. M. *J. Phys. Chem. B* **2006**, *110*, 14444.

(68) Köddermann, T.; Paschek, D.; Ludwig, R. *ChemPhysChem* **2007**, *17*, 2464.

(69) (a) Canongia Lopes, J. N.; Pádua, A. A. H. *J. Phys. Chem. B* **2006**, *110*, 7485. (b) Canongia Lopes, J. N.; Costa Gomes, M. F.; Pádua, A. A. H. *J. Phys. Chem. B* **2006**, *110*, 16816.

(70) Lynden-Bell, R. M.; Young, T. G. A. *J. Phys.: Condens. Matter* **2009**, *21*, 424120.

(71) Gray-Weale, A. *Aust. J. Chem.* **2009**, *62*, 288.

(72) Yan, T.; Burnham, C. J.; Del Pópolo, M. G.; Voth, G. A. *J. Phys. Chem. B* **2004**, *108*, 11877.

(73) Jiang, W.; Yan, T.; Wang, Y.; Voth, G. A. *J. Phys. Chem. B* **2008**, *112*, 3121.

(74) Yan, T.; Li, S.; Jiang, W.; Gao, X. P.; Xiang, B.; Voth, G. A. *J. Phys. Chem. B* **2006**, *110*, 1800.

(75) Smith, G. D.; Borodin, O.; Li, L.; Kim, H.; Liu, Q.; Bara, J. E.; Gin, D. L.; Nobel, R. *Phys. Chem. Chem. Phys.* **2008**, *10*, 6301.

(76) Borodin, O. *J. Phys. Chem. B* **2009**, *113*, 11463.

(77) Picálek, J.; Minofar, B.; Kolafa, J.; Jungwirth, P. *Phys. Chem. Chem. Phys.* **2008**, *10*, 5765.

(78) Tanaka, M.; Siehl, H.-U. *Chem. Phys. Lett.* **2008**, *457*, 263.

(79) Chang, T. M.; Dang, L. X. *J. Phys. Chem. A* **2009**, *113*, 2027.

(80) Nakano, H.; Yamamoto, T.; Kato, S. *J. Chem. Phys.* **2010**, *132*, 044106.

(81) Hansen, J.-P.; McDonald, I. R. *The Theory of Simple Liquids*, 2nd ed.; Academic Press: San Diego, 1986.

(82) Wilson, M.; Madden, P. A. *Phys. Rev. Lett.* **1996**, *77*, 4023.

(83) (a) Madden, P. A.; Wilson, M. *J. Phys.: Condens. Matter* **2000**, *12*, A95. (b) Ribeiro, M. C. C. *Phys. Rev. B* **2001**, *65*, 094205.

(84) Iuchi, S.; Izvekov, S.; Voth, G. A. *J. Chem. Phys.* **2007**, *126*, 124505.

(85) (a) Lynden-Bell, R. M. *Electrochem. Commun.* **2007**, *9*, 1857. (b) Lynden-Bell, R. M. *J. Phys. Chem. B* **2007**, *111*, 10800. (c) Lynden-

Bell, R. M. *J. Chem. Phys.* **2008**, *129*, 204503. (d) Streeter, I.; Lynden-Bell, R. M.; Compton, R. G. *J. Phys. Chem. B* **2008**, *112*, 14538.

(86) Margulis, C. J. *Mol. Phys.* **2004**, *102*, 829.

(87) Koel, M. *Proc. Estonian Acad. Sci. Chem.* **2000**, *49*, 145.

(88) Wilson, M.; Madden, P. A. *J. Condens. Matter* **1999**, *11*, A237.

(89) Zhao, W.; Leroy, F.; Heggen, B.; Zahn, S.; Kirchner, B.; Balasubramanian, S.; Müller-Plathe, F. *J. Am. Chem. Soc.* **2009**, *131*, 15825.

(90) Boon, J. P.; Yip, S. *Molecular Hydrodyamics*; Dover: New York, 1991.

(91) Sethfest, H. *Comm. ACM* **1970**, *13* (47), 624.

(92) Margulis, C. J.; Stern, H. A.; Berne, B. J. *J. Phys. Chem. B* **2002**, *106*, 12017.

(93) Berne, B. J.; Pecora, R. *Dynamic Light Scattering*; Wiley: New York, 1976.

(94) Frenkel, D.; McTague, J. P. *J. Chem. Phys.* **1980**, *72*, 2801.

(95) Ladanyi, B. M.; Liang, Y. Q. *J. Chem. Phys.* **1995**, *103*, 6325.

(96) Paolantoni, M.; Ladanyi, B. *J. Chem. Phys.* **2002**, *117*, 3856.

(97) Saito, S.; Ohmine, I. *J. Chem. Phys.* **1997**, *106*, 4889.

(98) Bursulaya, B. D.; Kim, H. J. *J. Phys. Chem. B* **1997**, *101*, 10994.

(99) Fecko, C. J.; Eaves, J. D.; Tokmakoff, A. *J. Chem. Phys.* **2002**, *117*, 1139.

(100) Tokmakoff, A. *J. Chem. Phys.* **1996**, *105*, 1.

(101) Dhar, L.; Rogers, J. A.; Nelson, K. A. *Chem. Rev.* **1994**, *94*, 157. (b) Farrer, R. A.; Fourkas, J. T. *Acc. Chem. Res.* **2003**, *36*, 605.

(102) Madden, P. A.; O'Sullivan, K. F. *J. Chem. Phys.* **1991**, *95*, 1980.

(103) By utilizing the polarizable forcefield and the nonpolarizable forcefield in this study, we performed normal mode analysis on the geometry optimized single $EMIM^+$ ion. The assignment of normal mode vibrations is carried out by matching the peaks of the frequency in DOS with the closest normal mode frequency. It is found that the peak of the lower frequency bands shows a blue shift by $\sim 5-25$ cm^{-1}, compared with the gas phase normal mode analysis of the isolated ion, due to the interactions in the condensed phase.

(104) Gray-Weale, A.; Madden, P. A.; Wilson, M. *J. Chem. Phys.* **2000**, *113*, 6782.

(105) Lunkenheimer, P.; Loidl, A. *Phys. Rev. Lett.* **2003**, *91*, 207601.

(106) Iuchi, S.; Morita, A.; Kato, S. *J. Phys. Chem. B* **2002**, *106*, 3466.

(107) McQuarrie, D. A. *Statistical Mechanics*; Harper & Row: New York, 1976.

(108) Urahata, S. M.; Ribeiro, M. C. C. *J. Chem. Phys.* **2006**, *124*, 074513.

(109) (a) Noda, A.; Hayamizu, K.; Watanabe, M. *J. Phys. Chem. B* **2001**, *105*, 4603. (b) Every, H. A.; Bishop, A. G.; MacFarlane, D. R.; Orädd, G.; Forsyth, M. *J. Mater. Chem.* **2001**, *11*, 3031. (c) Tsuzuki, S.; Tokuda, H.; Hayamizu, K.; Watanabe, M. *J. Phys. Chem. B* **2005**, *109*, 16474.

(110) Löffler, G.; Schreiber, H.; Steinhauser, O. *J. Chem. Eng. Data* **1997**, *107*, 3135.

(111) (a) Smith, W. *CCP5 Information Quarterly* **1982**, *4*, 13. (b) Nymand, T. M.; Linse, P. *J. Chem. Phys.* **2000**, *112*, 6152. (c) Aguado, A.; Madden, P. A. *J. Chem. Phys.* **2003**, *119*, 7471.

(112) (a) Noid, W. G.; Chu, J.-W.; Ayton, G. S.; Krishna, V.; Izvekov, S.; Voth, G. A.; Das, A.; Andersen, H. C. *J. Chem. Phys.* **2008**, *128*, 244144. (b) Noid, W. G.; Liu, P.; Wang, Y.; Chu, J.-W.; Ayton, G. S.; Izvekov, S.; Andersen, H. C.; Voth, G. A. *J. Chem. Phys.* **2008**, *128*, 244115.

(113) Wang, Y.; Izvekov, S.; Yan, T.; Voth, G. A. *J. Phys. Chem. B* **2006**, *110*, 3564.

(114) Ailawadi, N. K.; Rahman, A.; Zwanzig, R. *Phys. Rev. A* **1971**, *4*, 1616.

(115) Levesque, D.; Verlet, L.; Kurkijarvi, J. *Phys. Rev. A* **1973**, *7*, 1690.

(116) Baldelli, S. *J. Phys. Chem. B* **2003**, *107*, 6148.

(117) Press, W. H.; Teukolsky, S. A.; Vetterling, W. T.; Flannery, B. P. *Numerical Recipes in Fortran*; Cambridge University Press: New York, 1992.

(118) (a) Jiang, W.; Wang, Y.; Yan, T.; Voth, G. A. *J. Phys. Chem. C* **2008**, *112*, 1132. (b) Siqueira, L. J. A.; Ribeiro, M. C. C. *J. Phys. Chem. B* **2009**, *113*, 1074.

(119) Seddon, K. R.; Stark, A.; Torres, M.-J. In *Clean Solvents: Alternative Media for Chemical Reactions and Processing*; Abraham, M., Moens, L., Eds.; ACS Symposium Series 819; Americal Chemical Society: Washington DC, 2002.

(120) Brookes, R.; Davies, A.; Ketwaroo, G.; Madden, P. A. *J. Phys. Chem. B* **2005**, *109*, 6485.

(121) Köddermann, T.; Ludwig, R.; Paschek, D. *ChemPhysChem* **2008**, *9*, 1851.

(122) Zhao, W.; Leroy, F.; Balasubramanian, S.; Müller-Plathe, F. *J. Phys. Chem. B* **2008**, *112*, 8129.

(123) Borodin, O.; Smith, G. D.; Kim, H. *J. Phys. Chem. B* **2009**, *113*, 4771.

JP908914D